universität wien

MASTERARBEIT / MASTER'S THESIS

Titel der Masterarbeit / Title of the Master's Thesis

„Particle Number Size Distribution and Counting Efficiency of Polyethylene Terephthalate nanoplastics“

verfasst von / submitted by

Gregor Lattner, BSc

angestrebter akademischer Grad / in partial fulfilment of the requirements for the degree of

Master of Science (MSc)

Wien, 2021 / Vienna, 2021

Studienkennzahl lt. Studienblatt / degree programme code as it appears on the student record sheet:	UA 066 876
Studienrichtung lt. Studienblatt / degree programme as it appears on the student record sheet:	Masterstudium Physik
Betreut von / Supervisor:	Assoz. Prof. Dr. Paul Winkler, Privatdoz.

Acknowledgments

I would like to thank Assoz. Prof. Dr. Paul Winkler for allowing me to write my master's thesis in a topic as interesting and undiscovered as this. I owe great thanks to him for supervising my thesis and for lending me his ear for all the problems that came up, especially at the beginning when things did not go as smoothly as planned.
Furthermore I want to express my gratitude for Peter Wlastis, who I was in contact with seemingly every day and who was a huge help for the day-to-day problems that seemed to increase instead of decrease. Without his patience and advises I would probably still be in the laboratory working on this thesis.
I also want to thank Klara Maggauer for our time together in the lab, for helping me when it came to coding and for giving me new recipes I cook every week now.
A very special thank you goes out to all my colleagues I got to know during the years at the University, especially the ones that got very close to me as the years went by. I am very lucky we met and that you became dearest friends to me. I will never forget the days we spent on the 5th floor of our faculty agonizing about exercises or upcoming exams. Without you I am sure I couldn't have managed my study the way I did.

Lastly I want to thank my parents and my family for always believing in me when I told them I want to study a rather unconventional field and for supporting me in every way they could. Thank you for knowing what was best for me, especially when I did not. Who would have thought I could make it this far? I certainly had doubts.

Contents

Abstract

During the past 40 years, the production of plastic has increased 25 times leading to a growing concentration of plastic all over the planet. Recent studies have shown that plastic debris can eventually decompose into smaller plastic pieces in the micro - and even the nanometer scale. However, the amount of research on especially nanoplastic is still relatively small, making an increased number of measurements necessary.
There are several types of plastics used for a large number of different applications such as polypropylene (PP) commonly used for packaging products, low density polyethylene (LDPE) commonly used for grocery bags and plastic bags or polyethylene terephthalate (PET) commonly used for water bottles or fleece garment. This brings me to the main question of my Master's Thesis:

What are the particle number size distributions of polyethylene terephthalate (PET) when heated at different temperatures and what are the counting efficiencies of different devices when measuring PET nanoplastic aerosols?

To answer this question, Polyethylene Terephthalate (PET) plastic pellets were heated in a tube furnace and the concentration of the produced particles was measured.
The used devices were two Condensation Particle Counters (CPCs) with different working fluids (water and n-butanol) and a Faraday Cup Electrometer (FCE). These are some of the most important and common devices to measure particles in the nanometer (10^{-9} m) range.
The results not only show that nanoplastic can be produced by heating clean pellets in a controlled environment, but also that large concentrations in a broad size range (2 nm - 54 nm) can be found. Furthermore, the counting efficiency of the different CPCs reveal important properties of the PET in terms of its polarity.

Zusammenfassung

In den letzten 40 Jahren hat sich die Plastikproduktion um ein 25-faches gesteigert. Das führt zu einer wachsenden Ansammlung an Plastik auf dem ganzen Planeten. Neueste Studien zeigen, dass Plastikstücke in kleine Teilchen im Mikro - und sogar Nanometerbereich zerfallen können. Allerdings ist die Forschung auf dem Gebiet von Nanoplastik noch relativ jung, was eine wachsende Anzahl an Messungen notwendig macht.
Das bringt mich zu der Hauptfrage meiner Masterarbeit:

Was sind die Größenverteilungen von Polyethylene Terephthalate (PET) wenn man es auf verschiedene Temperaturen erhitzt und was sind die Messeffizienzen von verschiedenen Geräten wenn sie PET Nanoplastik-Aerosole messen?

Um diese Frage zu beantworten, wurden Polyethylene Terephthalate (PET) Pellets in einem Ofen erhitzt und die dabei entstandene Konzentration der Partikel gemessen.
Die verwendeten Geräte waren zwei Condensation Particle Counters (CPCs) mit verschiedenen Kondensationsflüssigkeiten (Wasser und n-Butanol) und ein Faraday Cup Elektrometer (FCE). Diese Geräte sind die mitunter wichtigsten um Partikel im Nanometerbereich (10^{-9} m) zu messen.
Die Ergebnisse zeigen nicht nur, dass Nanoplastik beim Erhitzen von sauberen Pellets in einer kontrollierten Umgebung produziert werden kann, sondern auch, dass hohe Konzentrationen in einem breiten Größenbereich (2 nm - 54 nm) detektiert werden können. Außerdem gibt die Messeffizienz der verschiedenen CPCs wichtige Eigenschaften bezüglich der Polarität von PET preis.

1 Introduction

In a very general way, aerosols are a suspension of solid or liquid particles in a carrier gas. In most cases, this carrier gas is air. The particles can cover a very broad size range, spanning from < 2 nm to over 100 μm [1].
Aerosols can be found all over the globe and can have different origins. They can also have a big influence on our climate as well as the human body and its health. Studies have shown that ultrafine particles (< 100 nm) can penetrate into the lung and reach other organs like the heart or the brain due to their small size [2] [3]. Furthermore, aerosols can travel large distances all around the world, making it a global problem [4].

One origin of aerosols is plastic. Plastics are heavily manifested in our everyday lives and not one day goes by in which we don't use or touch any product that is not made of or at least contains plastics of any kind. Whether it is the Smartphone we use, the clothes we wear or the bottle we drink our water out of, our lives would not be the same without it.
However, a huge percentage of the produced plastic ends up in the environment [5]. Due to chemical or biological degradation, it can become smaller over time and eventually reach a size in the micro - or even nanometer range [6][7]. When these particles get carried by a carrier gas, they become nanoplastic aerosols.
Even though the impact of plastics with such small diameters is not fully understood, there has been an increasing number of publications on this topic. Studies have found nanoplastics in regions far away from civilization, i.e. the antarctic [8], further emphasizing the aerosol characteristic nanoplastic can have.
The aim of this thesis is to further increase knowledge about nanoplastics, especially in terms of plastic degradation and the production of nanoplastics when heated in a controlled environment.
The measured particle number size distribution gives insight on how many nanoplastic particles can be produced this way and what their diameters are.

2 Plastics

Per definition, plastics are a wide range of different of synthetic materials that have polymers as a main ingredient. In general, a polymer consists of individual molecules, so called 'monomers' with the ability to covalently bond together into long chains [9].
In commercially available plastics, the polymer chains consist of 10^4 to 10^8 monomers [10].

Polymers can be divided into two different categories:
The first are *thermoplastics* with the ability to melt upon heating and harden upon cooling. One of the main properties of thermoplastics is that these processes can be reversed and redone at will. When softened by heating, thermoplastics can be reshaped. Some of the most common thermoplastics are polypropylen (PP), polyethylene (PE) and polyethylene terephthalate (PET), which was used for the measurements in this thesis [9].

The second kind of polymers are called *thermosets*, whose heating and cooling processes are not reversible since they undergo chemical reactions during those processes [9]. Examples for thermosets are polyurethane (PUR), vinyl esters or silicone [5].

2.1 PET

PET is probably best known for its use in water and other beverage bottles. Also, it is used in clothing such as in fleece garments, where it is known under the name polyester [10]. Some of the most important properties of polyethylene terephthalate for this thesis are summarized in Table 1.

The PET plastic used in the following experiments were in pellet form and bought from *Sigma Aldrich*. The product number of the pellets is 429252-250G.
Furthermore, they contain 30% glass particles as reinforcer [11].
Glass has a melting point of about 700°C - 800°C [14], with the exact value depending on

Table 1: Table of PET properties

Chemical Formula	$(C_{10}H_8O_4)_n$ [10]
Monomer	Terephthalic acid, Ethylene glycol [10]
Density	1.68 g/cm^3 (at 25°C) [11]
Melting Temperature t_m	250-255°C [11]
Share in global plastic waste	7.9% [5]
relative dielectric constant ε	$\varepsilon = 3.4$ [12]

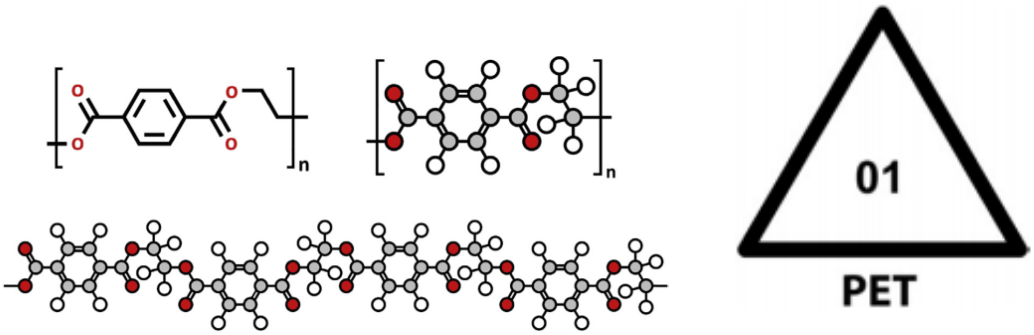

(a) Molecular structure of PET (b) Resin code of PET

Figure 1: The left figure (a) shows the molecular structure of PET. The grey dots represent the carbon atoms, the white dots represent the hydrogen atoms and the red dots represent the oxygen atoms. the 'n' in the upper two pictures stand for the iterations one monomer $C_{10}H_8O_4$ can have. One example of n = 4 can be seen in the lower picture [10]. The right figure (b) depicts the resin code of PET [10]. This code identifies the plastic used for a specific product [13].

the glass type. Since the melting temperature of any glass is way beyond the temperatures used in these experiments, it was not expected that the reinforcer glass particles started to melt or create unwanted particles in the measured range, hence altering the results.

2.2 Nanoplastics

Since there is currently no universal definition of what a nanoplastic is, in this thesis the definition proposed by Gigault et.al. (2018) [15] is used. Per this definition, a nanoplastic is a plastic particle in the size range of 1 nm - 1000 nm. They also propose that a nanoplastic is a particle originating from the degradation of larger plastic objects, which

is the case in this thesis.

This means that a clear distinction from nanomaterials has to be made, since according to the International Standard Organization ISO, a manufactured nanomaterial is "intentionally produced for commercial purposes to have specific properties or specific composition" [15][16].

In general, nanoplastic can be distinguished into two categories: primary and secondary nanoplastics.

Primary nanoplastics are directly produced for a variety of products such as cosmetic and cleaning products or tires [17]. A study has also shown the production of nanoparticles coming from 3D-Printers [18].

Secondary nanoplastics are produced when larger polymers including microplastics degrade into smaller pieces due to i.e. UV-radiation or oxidation, as shown by Lambert et.al.[6]. Microplastic has been found all around the world in places far away from civilisation such as the arctic [19], the antarctic [20] and in seafloor sediments [21], which shows that plastic debris can travel large distances from its original place of disposal.

Due to the eventual degradation of said plastics, one can assume that plastic in the nanometer range can be found in these places eventually.

Still, the research on nanoplastic is rather difficult to do, since it is hard to detect because of the small size of the particles. Nonetheless, there has been a number of studies in recent years such as by Lambert et.al.[6], Dawson et.al.[8] or Ter Halle et.al.[22], who characterized nanoplastics during the degradation of a PS coffee cup lid, turned microplastics into nanoplastics through digestive fragmentation by Antarctic krill and found nanoplastic in the North Atlantic Subtropical Gyre, respectively.

However, experiments that investigate the detection and characterization of aerosolized nanoplastics has been missing. The intention of this thesis is to deliver a detailed look at aerosol nanoparticles from PET.

2.3 Plastic Pollution

The reasons for the wide use of plastics are not hard to find: it is cheap to produce, easy to put in any shape or form and can be colored at will. Furthermore, the plastic industry has a big economic influence. It gives employment to more than 1.56 million people in over 55 000 Companies and has a turnover of more than 350 billion € (2019) in Europe [5].

The big disadvantages of plastic lay within its produced waste and the following pollution. In 2019, global plastic production reached 386 millionen tonnes, which is a rise from 359 million tonnes in 2018. Europe (EU28+NOR/CH) has produced 57.9 million tonnes of plastic in 2019 which is a decline of 6.4% from 2018. The european demand of plastic is 50.7 million tonnes, while the rest of the produced plastic is exported.
However, the collected plastic post-consumer waste has only been 29.1 Mt. 42.6% of that is being used for energy recovery, 32.5% is recycled and the rest (24.0%) is used as landfill [5].
That means that in Europe alone 36 Mt are either not collected or end up as landfill, which means it will eventually find its way into the environment.

Plastic released into the environment can degrade into smaller and smaller pieces [23] until it eventually reaches the nanometer scale [6][7].
The main issue with such small plastic particles is that it can possibly have a big impact on the environment - especially on the marine environment and on the health of both humans and animals.

2.3.1 Effects on Health

Nanoplastic particles that entered the human body can be transported to secondary organs via the bloodstream. Studies have shown that polystyrene (PS) nanoparticles can penetrate into red blood cells. This allows these particles to increase their circulation time in the body since it avoids a rapid clearence in the liver [24] [25].

Yan et.al. demonstrated that PS particles with 20 nm diameter can surpass the blood-brain barrier of rats [26]. Another study assessed the neurobehaviour of rats when exposed to PS nanoparticles for 5 weeks. In the study no significant changes in behaviour were observed [27]. Similar experiments on humans have not been conducted. Despite the unambiguous results and lack of studies on humans it gives an impression of how dangerous these particles can possibly be.
In vitro studies with human cell lines have shown that nanoplastic particles can activate the innate immune system, induce inflammatory respones or mediate oxidative stress [28]. However, there is a lack of long term studies and studies with nanoparticles coming from PE, PET and PP. Since all these in vitro studies have been performed with PS nanoparticles, an extrapolation to other plastics has to be treated with caution and further experiments have to be done in order to make conclusions.

Nanoplastics can be taken up by the body via either oral inhalation, absorption by the skin or ingestion, with the latter probably being the primary route to enter the body [28]. The reason for this is that microplastics have been found in various food and drinks, leading to human exposure. Some of these products include seafood like fish or shrimps, salt, sugar and beer [29] [30] [31] [32] [33] [34]. In addition, microplastics have been found in tap water and bottled water stemming from different sources around the world. The study has shown that out of 159 tap water samples, 81% contained microplastic particles [35]. Out of 259 water bottles from 11 different brands, 93% were contaminated with microplastic with an average of 10.4 particles/liter. Most of the contamination came from PP (54%) likely coming from the packaging or bottling process [36].
According to a study by Senathirajah et.al., a person consumes up to 5.5 grams of plastics per week, coming from different sources with the biggest source being drinking water with about 90% [37].
Even if these studies have been done with plastics in the micrometer range, a similar contamination with nanoplastic is entirely possible.
A deep penetration by nanoplastics into the human skin seems rather unlikely according

to a study by Alvarez-Roman et.al., who applied polystyrene (PS) particles with diameters of 20 nm and 200 nm to a porcine skin model [38]. This result was confirmed by another study which found that the PS particles only penetrated about 2-3 μm into the skin surface [39].

Another dangerous source in connection with plastic are chemical additives coming from the plastics [28]. These are added in order to manipulate the flexibility, stability or color from the eventual plastic product. It is known that these chemicals leach out and affect organisms [40]. Another toxic part coming from plastics are the monomers, which are the building blocks to build the polymers. One notorious monomer is bisphenol A (BPA). BPA can induce metabolic diseases or have a negative impact on reproductive effects and the development of newborn babys [41] [42].

2.3.2 Effects on the Environment

Plastic is the main contributor for marine litter, with fractions varying between 60% - 80%, depending on the exact location where marine litter is researched [43]. It is estimated that more than 13 000 plastic pieces per square kilometer are floating in the ocean [44].

Most of that plastic is buoyant, but it can still sink to the bottom of the ocean by currents or heavy fouling. Once at the bottom, plastic can change the workings of ecosystems. The main sources of plastic pollution in the ocean are beach litter with 80 % and the fishing industry with 18% [44].

A study has shown that at least 267 marine species suffer from entanglement and ingestion of plastic debris [45] often resulting in death by suffocation or starvation [46].

Some other studies focused on the potential effects of nanoplastics on sea animals and plants. Since a nanoplastic particle is smaller than the average vegetal or animal's cell (10 - 30 μm)[47], it is suspected that they can translocate to inner organs [48] [49].

Different studies suggest that nanoplastics have a significant impact on fish. For example,

it has been shown that PS nanoparticles (d_p = 24 nm) promote weight loss, change the blood count of cholesterol and triglycerides and it took the fish more than twice as long to consume 95% of the food [50].

The accumulation of PS nanoparticles in zebrafish has been studied and it was shown that it can be found in the head, yolk sac, gall blader and several other different tissues in the fish [51][52][53][54], leading to hypoactivity of the fish [55]. Pitt et.al. found that PS NPs can be passed on the offspring of zebrafish but does not cause major physiological disturbances [52]. Another study found that PS nanoplastic alone has only minor effects on zebrafish embryos, however, in combination with gold ions it can have increased toxic effects [56].

Studies on the effects of NPs on algae have shown different results. Some have shown that nanoplastics were adsorbed on microalgae [57][58] but little to no increased mortality could be measured, some have observed reduction in algae growth [57][59]. Also, some have shown no affection in growth or toxicity due to nanoplastics [60][61] and some have shown different results for different algae under same exposure conditions [62].

Bhattachary et.al. have observed a decrease in photosynthesis which seemed to be caused by the light blocking effect of the adsorbed PS particles (d_p = 20 nm) [63].

An uptake of microplastics is unlikely since the particles are too big in size to penetrate the plant cell wall [64], however an uptake of nanoplastics (d_p = 20 - 40 nm) by plant cells has already been observed in tobacco plants [65].

Another study showed that PS NPs are taken up by cucumber plants in the roots, where they are eventually transported to the above ground parts of the plants like leaves and fruits. It was observed that the NPs have a great influence on the nutritional values of the cucumbers as the proteins increased and Fe, Mg and Ca decreased [66].

Another study with PS NPs found that in wheat (Triticum aestivum L.) growth parameters and chlorophyll content were increased but micronutrients were decreased [67].

3 Aerosol Physics Theory and Concepts Relevant for this Thesis

3.1 Saturation Ratio

In a volume with a mixture of gases, the *partial pressure* p_v is the pressure one component of the mixture would have if it would occupy the whole volume and no other gases or vapors would be present [1].

The *saturation vapor pressure* $p_s(T)$ is the pressure of a vapor or gas when it is in equilibrium with its condensed vapor [1]:

$$p_s(T) = \exp\left(16.7 - \frac{4060}{T - 37}\right) \text{kPa} \tag{1}$$

The ***saturation ratio*** S_R is the ratio of the partial pressure and the saturation vapor pressure [1]:

$$S_R = \frac{p_v}{p_s(T)} \tag{2}$$

If $S_R < 1$, which means that the partial pressure is smaller than the saturation pressure, the system is undersaturated. In this case there is more evaporation than condensation on the surface where vapor and its liquid phase meet.

If $S_R > 1$, then the system is supersaturated - there is more condensation than evaporation on the surface.

If is $S_R = 1$, the system in saturated and there is no net mass transfer - the vapor and the liquid phase are in equilibrium at the surface [1].

In most cases, supersaturation is achieved by cooling a saturated vapor. In this process p_v remains constant but $p_s(T)$ decreases with decreasing temperature.

One common way of cooling a vapor is by adiabatic expansion. This is done by a rapid expansion of the gas. The adiabatic expansion follows the relationship:

$$\frac{T_1}{T_2} = \left(\frac{v_1}{v_2}\right)^{\kappa - 1} \tag{3}$$

where T_1 and v_1 are the initial temperature and volume of the gas, T_2 and v_2 the temperature and volume after the expansion and κ is the specific heat ratio [1].

3.2 Kelvin Radius

The Kelvin radius r^* is the critical radius a particle needs to have in order to stay constant in size. If a particle is lager than r^* it grows by condensation. If it is smaller than r^* it evaporates [1].

The Kelvin radius r^* is given by the Kelvin equation[1]:

$$r^* = \frac{2\sigma}{n_l k_B T \ln(S_R)} \tag{4}$$

σ: surface tension of droplet

n_l: number of molecules per unit volume in bulk liquid

k_B: Boltzmann constant

T: Temperature in Kelvin

S_R: Saturation ratio

It is apparent in Equation 4, that with increasing saturation ratio S_R, the Kelvin radius decreases, making particle growth by condensation possible for smaller particles at higher supersaturated conditions.

3.3 Nucleation

The phase transformation from vapor to liquid is called condensation and it is the primary process of aerosol production and growth in nature [1]. This process can only occur in supersaturated vapors.

Nucleation is the first step of any phase transformation, including condensation. In the

case of condensation, nucleation takes place when small liquid nuclei form when the compound still is a vapor [68].

In principle, there are two different kinds of nucleation: The homogeneous nucleation and the heterogeneous nucleation. Homogeneous nucleation is a rare process that also needs very high supersaturation. On the other hand, heterogeneous nucleation needs a supersaturation of only a few percent in order to happen. However, foreign nuclei on which the nucleation can occur need to be present. This is also the nucleation process that is observable the most in nature and is responsible for effects such as the formation of clouds and rain [68].

The two different nucleation processes are described in more detail in the following sections:

3.3.1 Homogeneous Nucleation

When particles grow in size by themselves in a supersaturated vapor, meaning without the presence of condensation nuclei, it is called *homogeneous nucleation.*

Forces such as the Van-Der-Waals force form molecular clusters, regardless of the saturation ratio of the gas.

In an unsaturated vapor, these cluster are unstable and disintegrate. However, in a saturated vapor, the cluster concentration increases since the particles collide more frequently. Due to the high saturation, these clusters can become stable and grow. For this process a supersaturation $S_R > 2$ is mandatory [1].

Every produced cluster with i molecules is assigned a Gibbs potential ΔG_i. For every formation of a cluster, the energy necessary is calculated as such [68]:

$$\Delta G_i = \underbrace{(\mu_l - \mu_v)}_{-k_B T \ln S} i + 4\pi\sigma r^2 \tag{5}$$

Assuming spherically shaped clusters with radius r_i, the surface area A_i is defined as:

$$A_i = 4\pi r_i^2$$

hence:

$$r_i = \sqrt{\frac{A_i}{4\pi}}$$

The energy for the nucleation and resulting formation of a cluster is given by [68]:

$$\Delta G_{hom} = \underbrace{4\pi\sigma r_i^2}_{\Delta G_{surface}} - \underbrace{\frac{4\pi}{3} k_B T n_l \ln(S) r_i^3}_{\Delta G_{volume}} \tag{6}$$

n_l is the number of molecules per unit volume, σ is the surface tension of the liquid and r_i is the radius of the formed cluster.

The first term of the right hand side of Equation 6 is based on the surface of the cluster and the second term is based on the volume of the cluster. Thus, the necessary energy for ΔG strongly depends on the cluster radius [69].

By plugging in r^* (s. Equation 4) into Equation 6, one gets the critical energy barrier ΔG^*_{hom}:

$$\Delta G^*_{hom} = \frac{16\pi}{3} \frac{\sigma^3}{(n_l k_B T \ln(S))^2} \tag{7}$$

Connecting Equation 6 with the saturation ratio (s. Equation 2), it delivers a description of why clusters grow or evaporate [69]:

- if $S < 1$, a constant increase of energy is mandatory in order for the particle to form. Therefore formed cluster are not stable and evaporate
- if $S = 1$, then $\ln S = 0$ and the energy is only dependent of the surface term in Equation 6. In this case nucleation is still hindered and the cluster decomposes. ΔG follows a similar trajectory like in the case of $S < 1$.
- if $S > 1$, then the cluster has to overcome an energy barrier in order to get into a

stable state. This energy barrier is the critical Gibbs energy ΔG^* and the particle needs to have the corresponding critical Kelvin radius r^*.

This effect is illustrated in Figure 2:

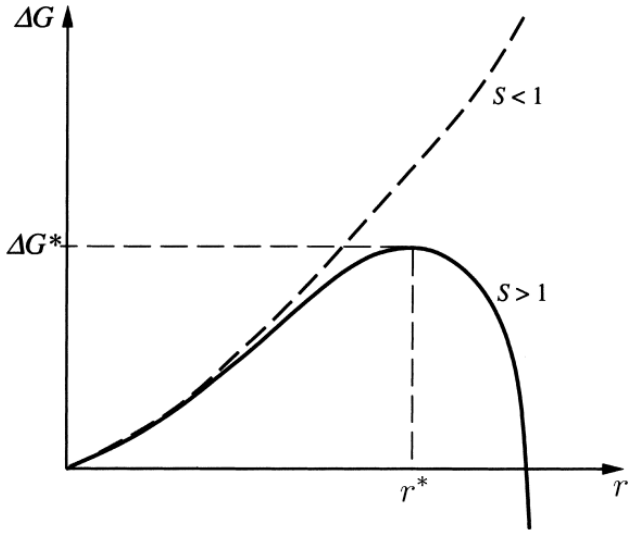

Figure 2: ΔG as a function of the particle radius r for both an unsaturated vapor $S < 1$ and a supersaturated vapor $S > 1$. [68]

This form of nucleation is an 'all-or-nothing phenomenon' and it is a steep function of S. [1].

3.3.2 Heterogeneous Nucleation

In comparison, the heterogeneous nucleation needs condensation nuclei or ions in order to occur. However, it can take place when the supersaturation is only a few percent - much less than for the homogeneous nucleation.

The condensation nuclei offer their surface on which the condensation of a vapor can take place [1].

There are multiple different cases of heterogeneous nucleation:

The first case is nucleation on *insoluble nuclei*.

At supersaturation, an insoluble nucleus has an adsorbed layer of vapor molecules on its surface.

The critical free energy ΔG^*_{het} for a cluster to form by heterogeneous nucleation on a flat

surface is:

$$\Delta G^*_{het} = \Delta G^*_{hom} \cdot f(m) \tag{8}$$

m is called contact parameter and is the cosine of the contact angle θ (s. Figure 3):

$$m = \cos\theta = \frac{\sigma_{SV} - \sigma_{SL}}{\sigma_{LV}} \tag{9}$$

σ is the surface tension and the respective indices stand for boundaries of the phases as seen in Figure 3.

$f(m)$ is given by:

$$f(m) = \frac{(2+m)\cdot(1-m)^2}{4} \tag{10}$$

$f(m)$ takes on values between 0 and 1. When $f(m) = 0$, then $\theta = 0°$ and $m = 1$, the wettability of the surface is maximal and the nucleation begins as soon as the vapor is supersaturated, meaning $\Delta G^* = 0$.

The other extreme case is when $f(m) = 1$, then $\theta = 180°$and $m = 0$. In this case, the wettability of the surface is minimal and homogeneous nucleation is more likely than heterogeneous nucleation [68] [69].

The process of a cluster formation on a flat surface can be seen in Figure 3.

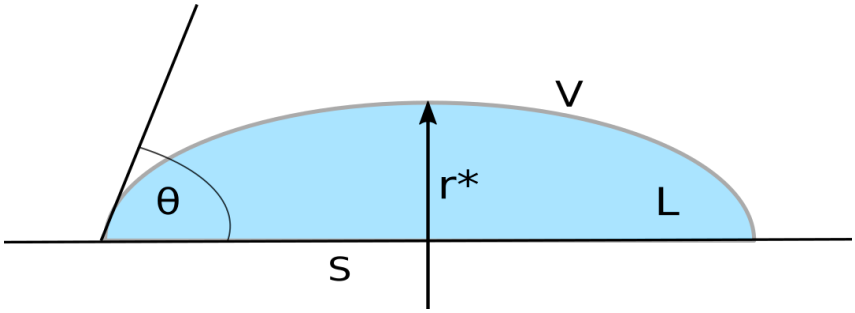

Figure 3: Schematic of heterogeneous nucleation on a flat surface. V indicates the vapor phase, L the liquid phase and S the solid phase. θ indicates the contact angle (based on [68] and [69])

Nucleation on a curved surface is described in similar way, however, the situation is more complex. In this case, not only the contact angle θ is relevant, but also the radius

of both the seed particle R_P and the critical radius r^* [68]:

$$\Delta G^*_{het,curv} = \Delta G^*_{hom} \cdot f(m,x) \tag{11}$$

with

$$f(m,x) = \frac{1}{2}\left[1 + \left(\frac{1-mx}{g}\right)^3 + x^3\left[2 - 3\left(\frac{x-m}{g}\right) + \left(\frac{x-m}{g}\right)^3\right] + 3mx^2\left(\frac{x-m}{g} - 1\right)\right] \tag{12}$$

where

$$g = \sqrt{1 + x^2 - 2mx} \tag{13}$$

and

$$x = \frac{R_P}{r^*}$$

The Kelvin equation for the critical radius r^* (s. Equation 4) also holds for heterogeneous nucleation [68].

A schematic of this process can be seen in Figure 4.

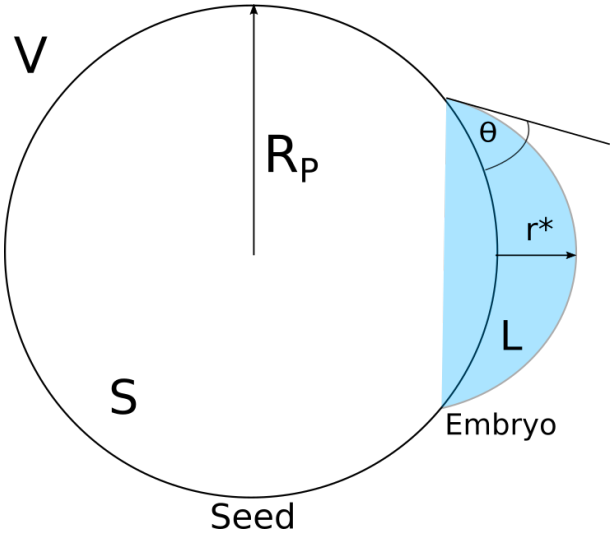

Figure 4: Heterogeneous nucleation on a curved surface. V, S and L represent the vapor, solid and liquid phase, respectively. R_P denotes the radius of the seed particle, r^* indicates the critical embryo radius and θ indicates the contact angle between the two particles (based on [68] and [69])

Another case of heterogeneous nucleation is on *soluble nuclei*:
The most common soluble nuclei in water come from sodium chloride (salt), originating from the ocean water. These nuclei are the main source of water droplets in the atmosphere because they allow particle growth at a supersaturation of a few percent. This is also the reason why supersaturation in nature hardly exceeds those few percent, since these nuclei consume all the excess vapor and therefore prevent higher supersaturations [1].

The effect of nucleation, especially the case of nucleation on a curved surface of insoluble nuclei is very important for this thesis. Since the measured particles are in a size range where they cannot be detected optically, the particles grow by condensation inside of the used devises, allowing them to be detected optically.

3.4 Coagulation

The process of aerosol particles colliding with each other is called *coagulation*. This results in the formation of larger particles and a decrease in total number concentration. When the motion of the particles is brownian, the coagulation is called *thermal coagulation*. This spontaneous phenomenon is present in every aerosol measurement.
An exact description is very complicated, especially for polydisperse aerosols like in this experiment. However, in most cases a simplified model is used to estimate the effect.
For monodisperse coagulation the following relations are important:

$$\frac{dN}{dt} = -K_0 N^2 \tag{14}$$

The rate of change of the number concentration with time dN/dt can be seen in Equation 14. This equation is true for particles with $d_p > 100$ nm K_0 is the coagulation coefficient [$m^3 s^{-1}$] and increases with decreasing particle size.
For particles smaller that 400 nm, K_0 has to be adjusted with a correction factor β. The

adjusted coagulation coefficient is then:

$$K = K_0 \beta \tag{15}$$

The correction factor approaches 1 for particles > 400 nm and decreases with the particle size [1].

Since this rate in Equation 14 is proportional to N^2, the coagulation is faster for larger concentrations and decreases for smaller concentrations.

Also, the particle concentration $N(t)$ changes at any point in time and is described as:

$$N(t) = \frac{N_0}{1 + N_0 K t} \tag{16}$$

where N_0 is the initial concentration and t is the time passed. This equation is useful for describing simple monodisperse coagulation with a constant K_0 [1].

The particles grow in size according to the following equation [1]:

$$\frac{d(t)}{d_0} = \left(\frac{N_0}{N(t)} \right)^{1/3} \tag{17}$$

This equation holds for liquid particles but is approximately correct for solid particles [1].

By plugging in Equation 16, one gets:

$$\frac{d(t)}{d_0} = (1 + N_0 K t)^{1/3} \tag{18}$$

where $d(t)$ is the particle diameter after a time t and d_0 is the initial particle diameter.

As already mentioned, the description of *polydisperse coagulation* is more complicated.

In the case of bidisperse aerosol, the coagulation coefficient $K_{1,2}$ is described as:

$$K_{1,2} = \pi(d_1 D_1 + d_1 D_2 + d_2 D_1 + d_2 D_2) \tag{19}$$

where d_1, d_2 are two different particle diameters and D_1, D_2 are their respective diffusion

coefficients.

If d_1 and d_2 vary in size, $K_{1,2}$ increases. This is because big particles have a large surface and slow diffusion and small particles have a small surface and fast diffusion. This combination allows the coagulation to happen more rapidly the bigger the difference in size of the particles is.

Hence, coagulation happens much faster for polydisperse aerosols than for monodisperse aerosols [1].

Even tough Equation 16 and Equation 17 are originally derived from the description of monodisperse aerosols, it is often used for polydisperse aerosols as well [1].

Coagulation is an effect that can be observed in the results of the following measurements.

3.5 Diffusion in Sampling Lines

Due to the Brownian motion, particles diffuse from areas with high concentration to areas with low concentration. Since the aerosol concentration close to the tube walls approaches 0, particles diffuse towards these walls, resulting in a lower measured particle concentration. The diffusive particle efficiency $\eta_{tube,diff}$ can be calculated as:

$$\eta_{tube,diff} = \exp(-\xi \cdot Sh) \tag{20}$$

$$\text{where:} \quad Sh = 3.66 + \frac{0.2672}{\xi + 0.10079 \cdot \xi^{1/3}} \tag{21}$$

$$\xi = \frac{\pi D L}{Q} \tag{22}$$

$$D = \frac{k_B T C_C}{3\pi \eta_{air} d_p} \tag{23}$$

Sh is called the Sherwood number, D is the particle diffusion coefficient, L is the tube length of the respective device, Q is the flow rate through the tube, and η_{air} is the viscosity of air [70].

Due to the settings in these measurements, $\eta_{tube,diff}$ is only a factor for small particles, as

it approaches 1 for $d_p \geq 5$ nm. Graphically, this can be seen in Figure 5:

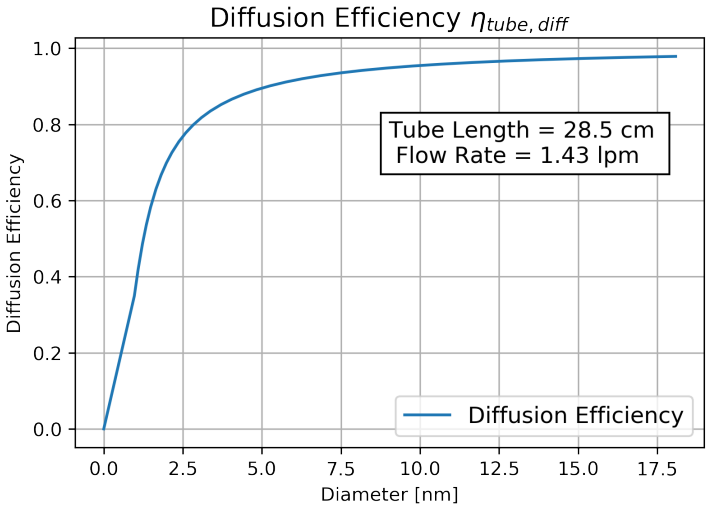

Figure 5: Diffusion Efficiency $\eta_{tube,diff}$ for the settings in these measurements

3.6 Size Distribution Function

The absolute aerosol concentration N_i for a size interval i can be written as:

$$N_i = n_i \Delta d_{p,i} \tag{24}$$

where n_i is the value of the aerosol distribution and $\Delta d_{p,i}$ is the size range of the particle diameter bin.

However, since these particle size intervals usually vary for each device, a direct comparison of size distributions is rather difficult and complicated to do.

To make things clearer while maintaining all information about the aerosol distribution, one can minimize the size bins to an infinitesimal size ($\Delta d_p \to 0$), resulting in $\Delta d_p = d(d_p)$. This results in:

$$\frac{n_i}{\Delta d_{p,i}} = \frac{n_i}{d_{p,i+1} - d_{p,i}} \Rightarrow \frac{dN}{d(d_p)} \tag{25}$$

In this case, the number size distribution becomes a continuous function of d_p and is no longer a discrete function [68].

A very common way in aerosol physics to describe the particle distribution as a function of $\log(d_p)$ instead of d_p. Since mathematically one cannot use the logarithm of a variable with a dimension, the following step has to be made [71]:

$$d\log(d_p) = \log(d_{p,u}) - \log(d_{p,l}) = \log\left(\frac{d_{p,u}}{d_{p,l}}\right) \tag{26}$$

where $d_{p,u}$ is the upper limit of the bin and $d_{p,l}$ is the lower limit of the bin.
Using this method, the units cancel out.
This results in the following particle size distribution $n_N(\log(d_p))$ [68]:

$$n_N(\log(d_p)) = \frac{dN}{d\log(d_p)} \tag{27}$$

which was used in this thesis.

3.7 Differential Mobility Analyzer (DMA)

The differential mobility analyzer (DMA) allows the classification of particles with a specific size from an aerosol with a broad spectrum of particle sizes. Thus, it serves as a source of monodisperse aerosol particles and makes the measurements of particle size distributions possible [72].
The DMA consists of two metal electrodes: one inner and one outer electrode. On the inner electrode a negative voltage between 0 V and -10^5 V is applied by a high-voltage module, creating an electric field in between the electrodes.
A schematic cross section of the used DMA can be seen in Figure 6. On one end, filtered particle-free sheath air Q_{sh} and the charged aerosol sample Q_a enter the DMA and flow in between the two electrodes. In this step it is important that the two laminar flows do not mix [73]. The particles with the selected electric mobility Z' reach the other end of the DMA where they exit via Q_s as a monodisperse aerosol into a particle counter. The remaining aerosol particles exit the DMA with the particle-free air via Q_{ex}. After being filtered, the air is pumped back into the DMA via Q_{sh} which means that this construction

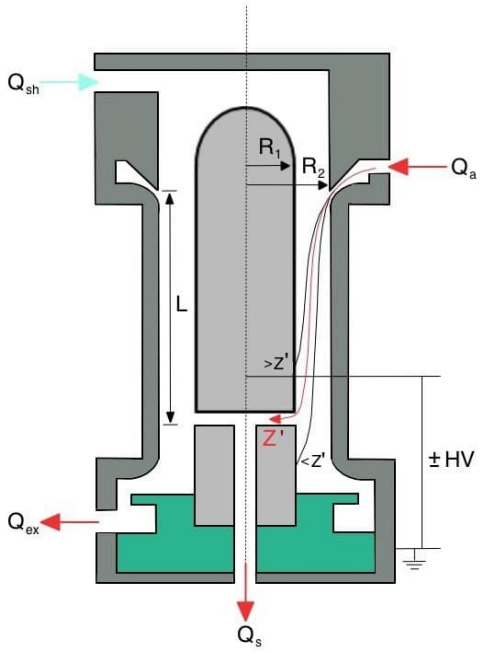

Figure 6: Vienna-type DMA cross-section schematic (by Dr. Gerhard Steiner [72], slightly modified for this thesis)

is a closed-loop arrangement. By varying the applied voltage in discrete steps the particle size distribution of the aerosol can be measured [74].

The DMA used in this experiment is a Vienna-type nano-DMA designed for diameters from 1 nm to $\approx$ 50 nm. The exact diameter range the DMA measures can be specified by adjusting the flows Q_a and Q_{sh}, Q_{ex}.

3.7.1 Electrical Mobility

The relation between the dimensions of the DMA and the characteristic electrical mobility Z is as follows [72]:

$$Z = \frac{Q_{sh} + Q_{ex}}{2} \cdot \frac{1}{2\pi LV} \ln\left(\frac{R_2}{R_1}\right) \tag{28}$$

were Q_{sh} is the sheath flow, Q_{ex} the exhaust flow, R_1 and R_2 are the respective radii of the inner and the outer electrode, L is the electrode length and V is the applied voltage.

For a fixed voltage, the electrical mobility Z' can be calculated by the flow rates [72]:

$$Z = \underbrace{\frac{Q_{sh} + Q_{ex}}{2}}_{Z'} \cdot \underbrace{\frac{1}{2\pi LV} \ln\left(\frac{R_2}{R_1}\right)}_{const.} \tag{29}$$

$$\Rightarrow Z' = Z \cdot \underbrace{\frac{2\pi LV}{\ln(R_2/R_1)}}_{const.} \tag{30}$$

$$\text{with } Z' = \frac{Q_{sh} + Q_{ex}}{2} \tag{31}$$

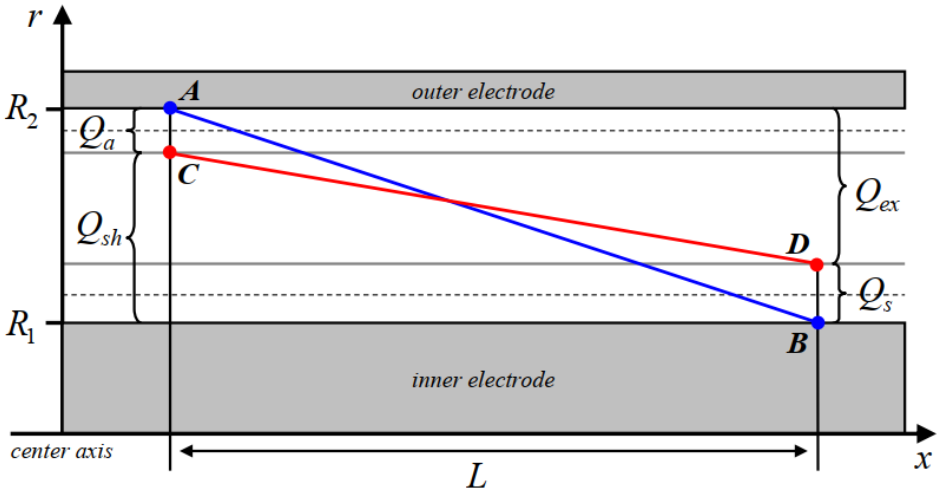

Figure 7: Trajectories of particles with a high mobility (blue line) and low mobility (red line) in a DMA [72]

In Figure 7, the trajectories of particles with different electrical mobilities can be seen when they pass through the DMA. For a set voltage, the particles with the highest mobility that can be transferred from the inlet Q_a to the outlet Q_s follow the blue line from point A to point B. The particles with the lowest mobilities that still reach the outlet follow the red trajectory from C to D [72].

Consequently, the maximum mobility is:

$$Z'_{max} = \int_B^A 2\pi \cdot r \cdot v(r) \cdot dr = Q_{sh} + Q_a = Q_{ex} + Q_s \tag{32}$$

This means that particles with a $Z' > Z'_{max}$ cannot reach the sample outlet since they

have a steeper trajectory than the blue one visible in Figure 7 and will be selected out by the DMA.

The minimum mobility is:

$$Z'_{min} = \int_D^C 2\pi \cdot r \cdot v(r) \cdot dr = Q_{sh} - Q_s = Q_{ex} - Q_a \tag{33}$$

Likewise, particles with a mobility $Z' < Z'_{min}$ and a flatter trajectory than the one from C to D cannot reach the sample outlet and will not be detected [72].

Hence, the mobility range that can be measured is:

$$Q_{sh} - Q_s \leq Z' \geq Q_{sh} + Q_a \tag{34}$$

Another way of expressing the mobility range is by [70]:

$$Z - \Delta Z \leq Z' \geq Z + \Delta Z \tag{35}$$

$$\text{where: } \Delta Z = Z\beta \tag{36}$$

β is the resolution of the DMA and is calculated as:

$$\beta = \frac{Q_s + Q_a}{Q_{sh} + Q_{ex}} \tag{37}$$

This implies that for a selected electrical mobility Z' the classified aerosol spans a range of different mobilities and therefore particle diameters as described in Equation 34 and Equation 35.

For the Vienna-type nano-DMA used in this experiment a resolution $\beta = 0.15$ was chosen.

The particle diameter is related to the electrical mobility via the Stokes' Law [74]:

$$d_p = \frac{neC_c(d_p)}{3\pi\eta Z} \tag{38}$$

where n is the number of elementary charge units, e is the elementary charge, C_c is the Cunningham slip correction factor and η is the viscosity of air (18.2 μPa·s).

The Cunningham slip correction factor C_c is needed in order to calculate the drag on smaller particles ($d_p < 100$ nm) or high Knudsen numbers, respectively. A good approximation for C_c, which was also used throughout this thesis, is the following [72]:

$$C_c(d_p) = 1.0 + 2.429 \cdot \frac{\lambda}{d_p} + 0.84 \cdot \frac{\lambda}{d_p} \cdot \exp\left(-0.43 \cdot \frac{d_p}{\lambda}\right) \tag{39}$$

where λ is the mean free path of air molecules (≈ 67 nm)

3.8 Aerosol Charger

In order for an aerosol particle to be classified and reach the sample outlet of a DMA, it needs to have an electric charge (s. Equation 38).
This is achieved by sending the irregularly charged aerosol through an aerosol charger (also called aerosol neutralizer), which leaves the aerosol with a well-defined steady state charge distribution, regardless of the initial charging state of the aerosol [75].
The charger used for these measurements was the *TSI Advanced Aerosol Neutralizer 3088*. With this charger, the charge distribution is achieved via bipolar diffusion. Ions of both positive and negative polarity are produced, and via diffusion, particles and ions interact and exchange charges.
This charger uses soft X-Ray radiation with an energy of <9.5 keV in order to produce these ions [76].

3.8.1 Charge Distribution

The charge distribution can be described by the Fuchs charge distribution model (1963) [77]. This effect comes from the collision of particles and ions, neutralizing initially charged particles and charging initially neutral particles [72].

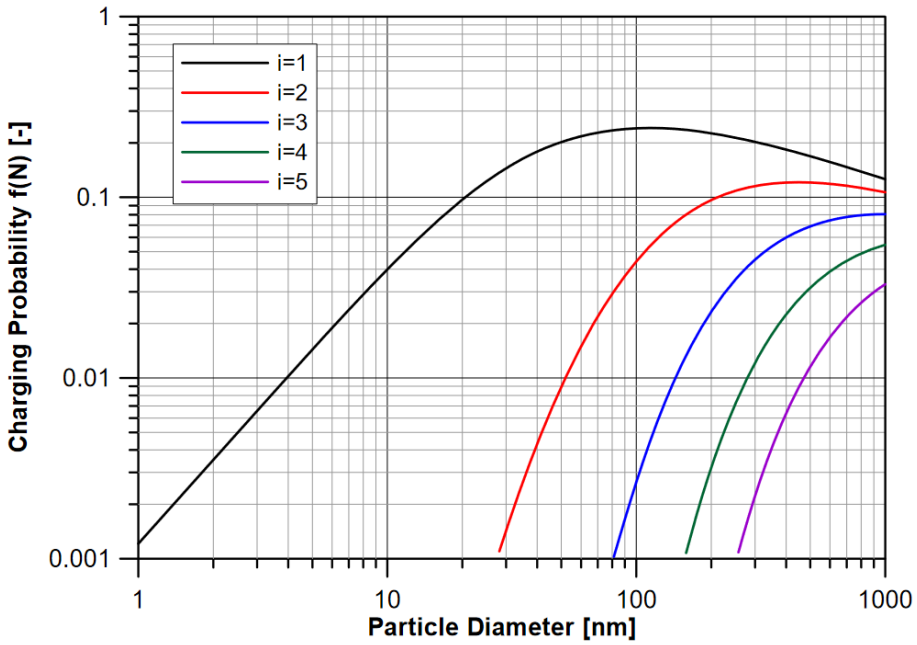

Figure 8: Charging probabilities for negatively charged aerosols with charging states i=1 to 5 according to the Fuchs' law [72]

In Figure 8, one can see the charging probabilities of negatively charged aerosol particles in a bipolar ionic atmosphere with charging states i ranging from 1 to 5, according to Fuchs' law. The illustration shows that the larger the particles are, the bigger the chance is for the particle to be multiply charged.

For the following experiments, the upper limit for the detection of particles was 54.6 nm, which means the charging probability for a doubly charged particle at the upper limit is about 0.01 and the probability for 3 or more charges is approaching 0. Therefore, no charge correction has been made, since for the most part only singly charged particles were expected. In addition to that, the majority of the detected particles were below 30 nm in diameter, which means that a charge of $i \geq 2$ is virtually 0%.

3.9 Condensation Particle Counter (CPC)

Ultrafine particles, which include those in the nanometer range, cannot be detected optically. By supersaturation of a working fluid and the following heterogeneous nucleation, those particles grow until they reach a size in the micrometer range (with the exact size

depending on the used device) until they can be detected optically. The final size of the particle is very uniform and almost independent of the initial size while the particle concentration remains the same.
In modern CPCs, the counting of the particles is done using light-scattering techniques. A light source hits the aerosol particles and the light waves get scattered in the process. The photodetector detects the scattered light and its intensity yields information about the particle concentration [1] [70].

For this thesis two different CPCs were used. The first one is the *TSI Model 3776* with n-butanol as the working fluid and the second one is the *TSI Model 3788* with water as the working fluid.

3.9.1 Butanol-based CPC

In the TSI 3776, the aerosol sample is drawn into a heated saturator where the aerosol particles are saturated with butanol. In the next step, the aerosol passes the condenser, in which the temperature is substantially lower than in the saturator. During this cooling procedure, $p_s(T)$ decreases faster than p_v and supersaturation of the aerosol stream is achieved (s. Equation 2). The supersaturated butanol condenses on the aerosol particles which serve as the condensation nuclei [69] [70] .
Once the condensed particles reach the Kelvin radius (s. Equation 4), they grow in size. An illustration of this process can be seen in Figure 9.
For the detection, they pass an optical detector where the scattered light is measured [78]. The TSI 3776 has a saturator temperature of 39°C and a condenser temperature of 10°C [79]. The schematic of the TSI 3776 is visible in Figure 10.

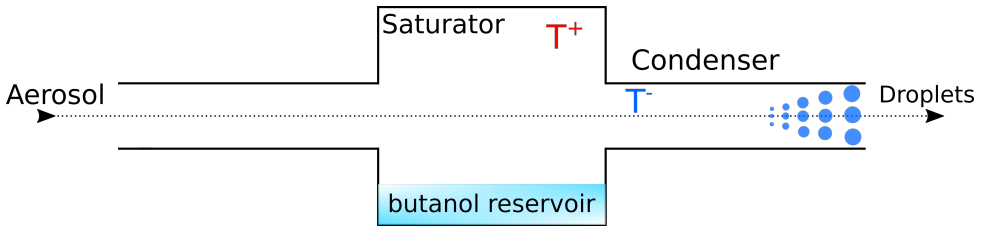

Figure 9: Schematic of the growth of particles inside a butanol CPC (based on P. Wlasits [69])

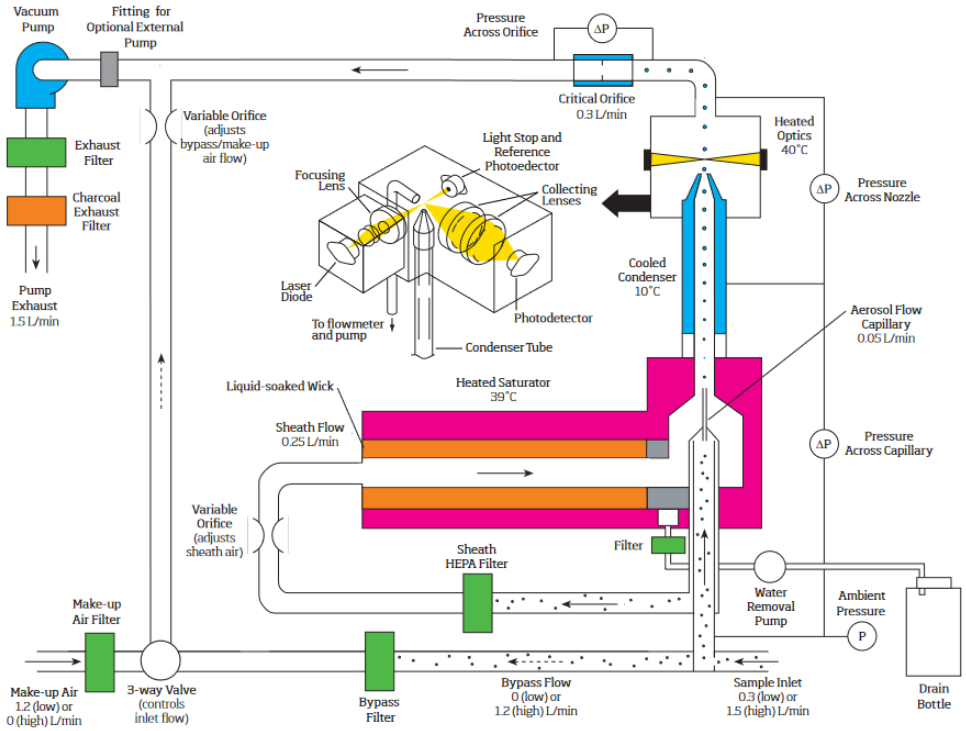

Figure 10: Schematic of the TSI Model 3776. An internal pump draws the aerosol sample into the CPC. The flow can be adjusted to either 1.5 lpm (high-flow mode) or 0.3 lpm (low-flow mode). The high-flow mode was used in the following measurement as it improves the response time of the CPC and minimizes particle transport loss. In either flow mode, 0.3 lpm of the inlet flow passes through the saturator and condenser, since in high-flow mode 1.2 lpm is diverted as a bypass flow. The particles then grow in size as described in section 3.9.1 in order to be detected optically [78].

3.9.2 Water-based CPC

The water-based CPC used in these experiments was the TSI 3788. The function principle is different than the one in the butanol CPC. Reason for this is that water has a higher mass diffusivity than butanol. So if one would simply change the working fluid from bu-

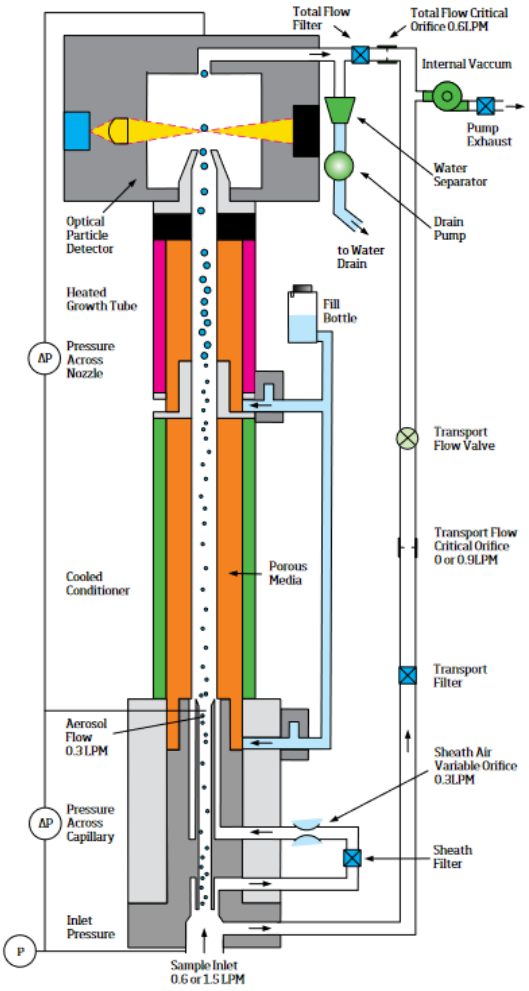

Figure 11: Schematic of the TSI Model 3788 [80]

tanol to water in the TSI 3776, the water vapor would diffuse to the walls of the condenser.

However, if a cold aerosol saturated with water vapor reaches a warm growth tube, the water vapor diffuses to the center of the tube at a faster rate than the heat that is transferred from the walls. That is because the water vapor has a higher thermal diffusivity than air [70].

The TSI 3788 is working on that principle. The aerosol probe is drawn through the inlet via the internal pump, operating at $\approx$ 1.5 lpm. Then, the sample reaches the cooling region where it is saturated with water vapor. The sample then passes the heated growth tube where the aerosol particles act as nuclei for heterogeneous condensation and the particles grow in size. An illustration of this process can be seen in Figure 12.

For the detection, the particles are passing the laser where the scattered light is measured [80]. The temperature of the cooling region is 15°C and the temperature of the growth tube is 75°C [81].

The whole schematic of the TSI 3788 can be seen in Figure 11.

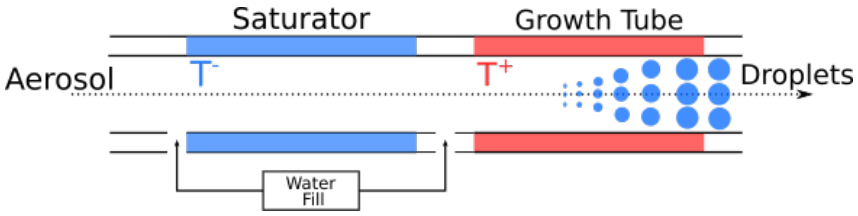

Figure 12: Schematic of the growth of particles inside a water CPC (based on [80])

3.10 Faraday Cup Electrometer (FCE)

Another way of measuring aerosol number concentration in the nanometer size range is via the Faraday Cup Electrometer (FCE). Unlike a CPC, the FCE can only measure charged particles. Since the aerosol stream passes a charger and a DMA the particles produced in this experiment can also be measured this way.

The charged aerosol is drawn into the FCE and an electrically isolated, high efficiency conductive filter inside a Faraday cup collects the particles. The cup then produces an induced charge equal to the one carried by the charged particles on the filter. The electrometer measures the resulting current I.

The current I is very small and in the magnitude of femtoamperes, hence this sort of particle detection is very sensitive and any minor exposure to an outside electric field can alter the results [70] [82].

When the current I is known, the resulting particle concentration can be calculated with the following equation [82]:

$$N = \frac{I}{n \cdot e \cdot Q_{FCE}} \tag{40}$$

where N is the aerosol particle concentration, I is the measured electrometer current, n is the number of charges per particle, e is the elementary unit of charge and Q_{FCE} is flow rate of the FCE.

The FCE used for this thesis was a *TSI Aerosol Electrometer Model 3068B*. It has a sensitivity of ±1 fA at 1 second averaging time (as in the following measurements) and covers a particle size range of 2 nm - 5 μm [82].

The schematic of the TSI 3068B can be seen in Figure 13

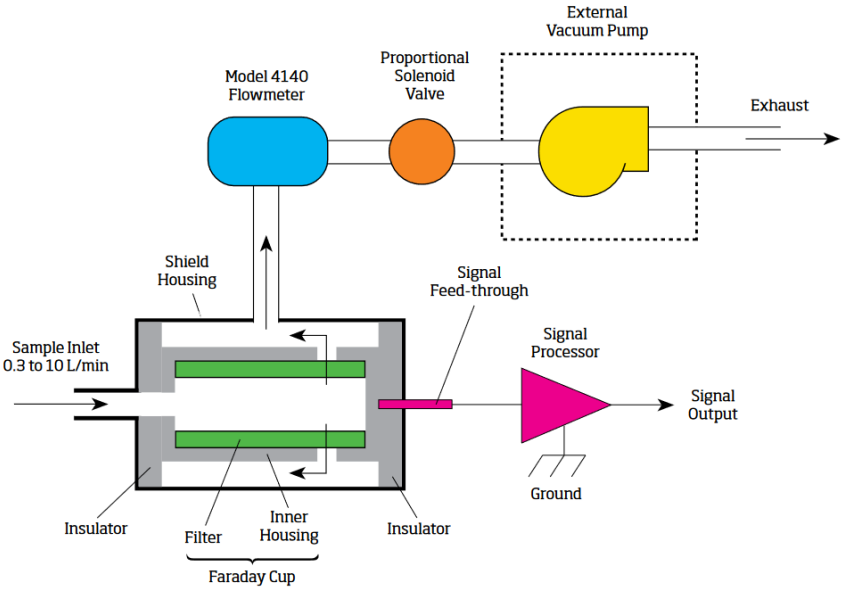

Figure 13: Schematic of the TSI 3068B. The aerosol sample is drawn into the FCE via the sample inlet. Then, the insulated filter collects the charged particles. This filter, together with the inner housing form the Faraday cup. The electrometer measures the electrical current I draining from the filter. The data for the measured concentration the reaches the signal processor. In the last step, the aerosol reaches the exhaust and its flow is regulated with a flowmeter and pumped through with an external vacuum pump [82].

3.11 Cutoff Diameter

In order to characterize a CPC, it is common to determine its detection efficiency η.

η gives insight on how well particles, especially small particles, are detected by the CPC. The detection efficiency depends on many factors, including the particle size, the particle material or on the used CPC.

This efficiency is determined by measuring the aerosol concentration N simultaneously with the CPC and the FCE and comparing the measured concentrations by calculating

the ratio:

$$\eta = \frac{N_{CPC}}{N_{FCE}} \tag{41}$$

The detection performance of a CPC is commonly described by the 50%-cutoff diameter $d_{p,50}$. This is the corresponding diameter where $\eta = 0.5$.

$$d_{p,50} = d_p(\eta = 0.5)$$

Hence, a lower cutoff diameter yields a better detection performance.

Below $d_{p,50}$, the efficiency decreases to 0, above $d_{p,50}$ the efficiency increases until it eventually reaches a plateau of 1 for larger particles, meaning the CPC and the FCE measure the same concentration from a certain diameter on.

Previous studies have shown that the cutoff-diameter depends on various factors such as the surface tension of the working fluid of the CPC [83], the charging state of the seed particle [84] or similarities between the seed particle and the working fluid in terms of polarity [85].

Consequently, the detection efficiency η has to be determined individually for each seeding particle material and working fluid under controlled laboratory conditions.

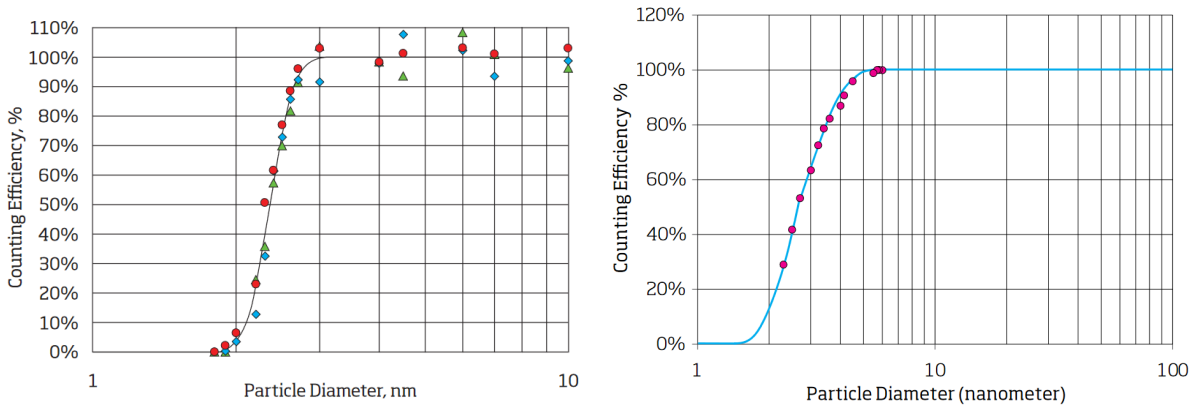

(a) Counting effeciency TSI 3776

(b) Counting efficiency TSI 3788

Figure 14: Typical counting efficiency curves for CPCs. The results of these particular curves come from sucrose particles and have been taken from the manuals of the respective CPCs. In the left plot, the differently colored symbols represent the data measured with three different TSI 3776's. [78][80]

3.11.1 Chemical Properties of the used materials

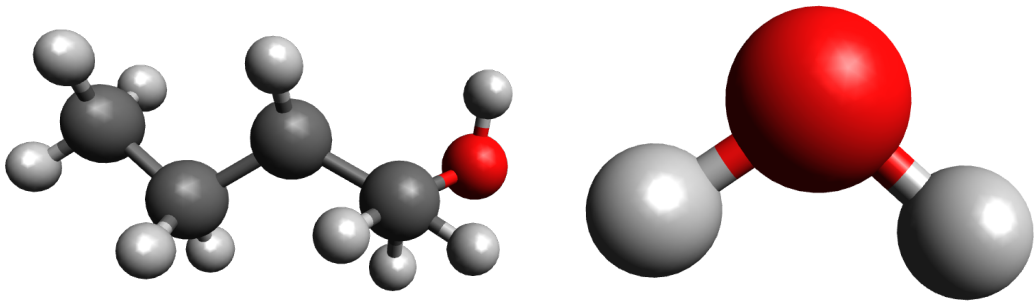

(a) Butanol C_4H_9OH (b) Water H_2O

Figure 15: Chemical properties of the two working fluids butanol and water. The graphics have been drawn using Avogadro [86]. The dark grey dots represent the carbon atoms, the light grey dots represent the hydrogen atoms and the red dots represent the oxygen atoms

The chemical properties of the used working fluids can be seen in Figure 15. An essential difference between these two fluids that is important for this thesis is their respective polarity.

In general, a polar molecule is a molecule with a permanent dipole moment. These molecules are formed by differences in the electronegativity of atoms in the molecule [87]. The polarity is measured by the electric dipole moment μ or the relative dielectric constant ε [69]. The properties in terms of polarity (at standard conditions) of the working fluids used in this experiment can be seen in Table 2.

Table 2: Properties of polarity of the working fluids [88]

Fluid	ε [ ]	$\mu \cdot 10^{-30}$ [Cm]
n-butanol	17.51	5.8
Water	78.36	6.2

From Table 2 it can be seen that water is a very polar fluid with a high relative dielectric constant and butanol features comparatively weak polarity.

PET has a relative dielectric constant of $\varepsilon = 3.4$ [12].

Previous studies by Wlasits et.al. ([69] [85]) have shown a strong dependency of the detection efficiency of a CPC and chemical similarities in terms of polarity between the

working fluid and the seed particles.

According to the authors, nonpolar fluids interact better with nonpolar seed particles, resulting in an increase of the detection efficiency.

Same thing with polar working fluids - they interact better with polar seed particles. Therefore the detection efficiency of a CPC with a polar fluid such as water increases when measuring polar seed particles.

4 Methodology and Setup

The aim of this thesis is to see under which conditions nanoplastics from PET pellets are created and how they vary in size and concentration, depending on three factors:

1. Temperature in the tube furnace
2. Air flow through the tube furnace
3. Time of the plastic in the tube furnace

The chosen temperatures inside the furnace were:

1. 180 °C
2. 190 °C
3. 200 °C

The reason why these temperatures were chosen was that prior to the measurements, an initial temperature had to be guessed and tried. Fortunately, a temperature where a lot of particles were produced was found rather quickly. The temperature of 180°C was the first temperature tried and particles in the magnitude of 10^5 p/cm^3 were produced after the PET pellets were in the tube furnace for 60 minutes (s. Figure 18). The temperature was then increased in 10°C steps in order to get three temperatures for each flow. Even though the selected temperatures are below the melting temperature t_m of the PET pellets (250°C - 255°C), a sufficiently high particle concentration was achieved and increasing the steps above the t_m was not considered as necessary.

Another reason for temperatures below t_m was that the pellets were put straight into a quartz glass spoon without any kind of protective layer between the spoon and the pellets. After the measurements were done, the pellets were in the spoon for over 100 minutes and have slightly burned into the spoon. The lower the temperature, the lower this effect was, resulting in temperatures that were chosen to be as low as possible while a sufficiently high nanpoparticle concentration was produced.

Initially, aluminum foil was used as a protective layer between the PET and the spoon,

but unfortunately this foil produced a high concentration of unwanted particles, eliminating this approach rather quickly.

The created particles were measured alternatively with the TSI 3788 and the TSI 3776.

The nanoplastic particles were selected in size by their electric mobility with a Vienna-type nano-DMA. The dimensions and flow properties of the DMA can be seen in Table 3. These settings allow a selection of particles in the range of 0 nm - 54.6 nm.

Table 3: Dimensions and flows of the used Vienna-type DMA

R_1	17.5 mm
R_2	24.1 mm
L	15 mm
Q_{sh}	(14.5 ± 0.2) lpm
Q_{ex}	(14.6 ± 0.2) lpm

However, the lower range limit 0 nm is more of a theoretical limit. Realistically, the lower detection limit is about 1 nm.

The DMA was operated in analyzer mode, in which the particle sizes were measured in 97 channels, ranging from 10 000 V to 0 V. One voltage/channel lasted for 7 seconds.

The voltages were set by the EMS-10 Control Center Operating Software EMSCC 1.4. One EMS run corresponds to the variation of the Voltages from 10 000 V to 0 V in 97 steps or channels and the particle concentration in the respective channel is measured.

The nanoplastic particles were then recorded via a laptop and the AIM (Aerosol Instrument Manager) software.

4.1 Preparation for Measurement

The schematic of the setup can be seen in Figure 16.

In the beginning of every day, the flows Q_F and Q_D, which are filtered particle free air, were adjusted with rotameters and measured with a gasmeter. This air acts as the carrier gas of the nanoplastic aerosol.

As discussed in section 3.7.1, the sum of Q_F and Q_D ($= Q_A$) was chosen in order to get

a DMA resolution of $\beta = 0.15$, resulting in the following three constellation of flows:

Table 4: Constellation of flows within this experiment with their respective uncertainties

Q_F [lpm]	Q_D [lpm]	Q_A [lpm]
0.8 ± 0.1	1.5 ± 0.1	2.3 ± 0.3
1.0 ± 0.1	1.3 ± 0.1	2.3 ± 0.3
1.2 ± 0.1	1.1 ± 0.1	2.3 ± 0.3

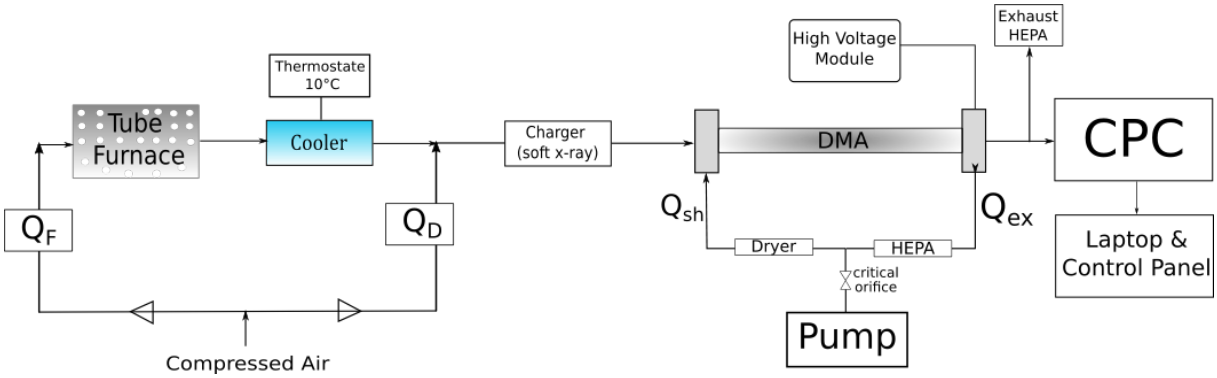

Figure 16: Schematic of the Experiment. The pellets are inserted in the tube furnace and get heated up. The produced nanoparticles then reach the cooler, which is set to 10°C. In the following stage the aerosol particles pass the x-ray charger, in order to be selected by their size in the DMA as a next step. The monodisperse aerosol then reaches the CPC. Before the CPC there is an exhaust flow as a precaution if any excess air is in the setup, which could damage the CPC. The flows Q_{sh} and Q_{ex} are set by the critical orifice.

After that, a background measurement of the used CPC was made to see if there are some unwanted particles somewhere in the setup.

The cooler in this experiment was a water based cooler made out of glass. The aerosol flows through a channel inside and is surrounded by water that is constantly pumped through the cooler and can be set to any desired temperature above 0°C. In this case the temperature was set to 10°C. Higher temperatures caused the plastic tubes to heat up and potentially produce unwanted particles.

When the cooler and the tube furnace have reached the desired temperature, the PET pellets were inserted into the middle of the furnace. The onset time t_0 that the plastic heated up before a measurement was chosen to be 60 minutes. The reason for t_0 being

60 minutes was that the longer the pellets were in the tube furnace, the more stabilized the produced particle concentration was (s. Figure 18).

Since every single pellet varies in mass, 3 pellets were weighed 10 times, resulting in an average mass for 3 PET pellets of:

$$m_{\text{pellets}} = (8.15 \pm 0.64) \cdot 10^{-2}\text{g}$$

The pellets were evenly distributed in the middle of a glass spoon and inserted into the tube furnace. The tube furnace used in these experiments was the *Carbolite EHA 12/150B* with a maximum heating zone of 1.50 cm [89] in the middle of the furnace tube. Hence, the spoon was put inside this zone to maximize the heating process. The schematic of the furnace and the placement of the pellets can be seen in Figure 17.

The right placement was checked by measuring the length of the stuck out part of the spoon.

After an eventual adjustment of the placement was made, the pellets were then heated up for $t_0 = 60$ minutes.

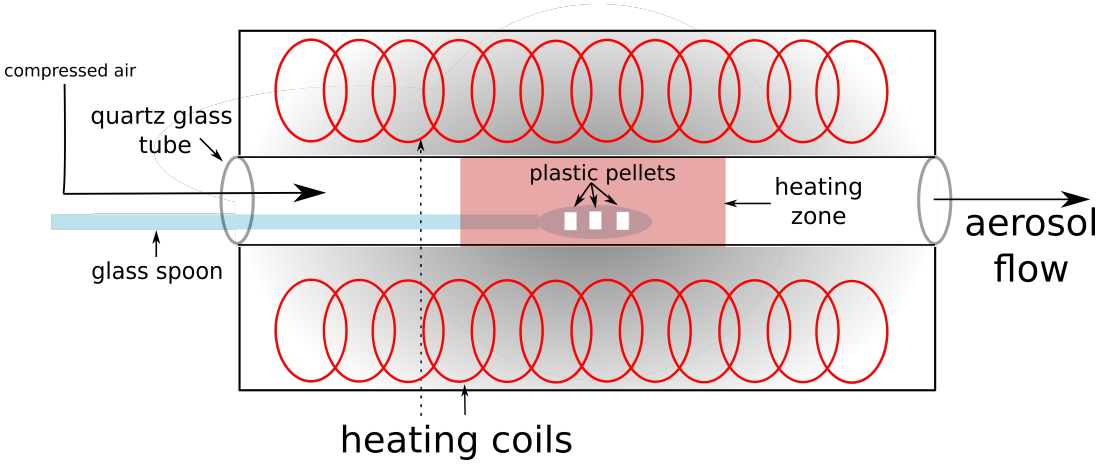

Figure 17: Schematic of the tube furnace and the heating process of the pellets

After t_0 has passed, the HV-module and the charger were turned on and 3 EMS-runs were recorded, lasting for about 40 minutes in total. After the measurement the pellets were put out of the furnace and a picture was taken. Since some rest particles were still in the spoon, the spoon was heated out at 350°C for about 20 minutes in order to fully

evaporate these particles.
After the furnace cooled down to the desired temperature for the next measurement, another 3 pellets were inserted into the spoon and the whole process started all over.
In total, 18 measurements were made, 9 for each CPC.

4.2 Data Collection

When t_0 has passed, the aerosol was sent into the DMA, the HV module was turned on and the EMS program was started. The particle concentrations were then recorded with the AIM software.
The number size distribution by the AIM was saved as a .csv file. The particle concentration for each channel was then averaged over the time period of one channel. For the number size distribution one channel lasted for 7 seconds, for the cutoff measurements the length was increased to 30 seconds.
In order to determine the exact particle diameters of each channel, the voltage in the DMA was used and converted to the particle diameter d_p via Equation 28 and Equation 38. The voltages were read out by the EMS software.

4.3 Uncertainty Estimations

Since the flows Q_F and Q_D were measured with a gasmeter, the smallest increment was taken as the uncertainty. This results in an uncertainty of the measured flows Q_F and Q_D of $\pm$ 0.1 lpm. The uncertainty of Q_A was then determined by Gaussian propagation of uncertainty. These flows and their respective uncertainties can be seen in Table 4.

The reason why the relative uncertainties of Q_{sh} and Q_{ex} in Table 3 and Table 13 are lower than in Table 4 is because Q_F and Q_D were measured with a *Gilibrator - 2* flowmeter and not the gasmeter. This flowmeter has an uncertainty of $\pm$ 1% [90], which is lower than the uncertainty of the gasmeter. For both Q_{sh} and Q_{ex} a series of 12 measurements have been made and the uncertainties were calculated by the Gaussian propagation of

uncertainty.

All the other uncertainties are summarized in Table 5:

Table 5: Uncertainty estimations of all the significant terms in this measurement

$\Delta T_{\text{Furnace}}$	$\pm$ 5°C
Δt_0	$\pm$ 2 min
$\Delta N_{\text{TSI 3788}}$	$\pm$ 10% [80]
$\Delta N_{\text{TSI 3776}}$	$\pm$ 10% [78]
ΔN_{FCE}	$\pm$ 1 fA [82]
Δd_p	$\pm$ 15%

The uncertainty estimations for the particle concentrations of the used devices were taken from the respective user manual. Δt_0 is a simple estimation because there often were deviations of how much time t_0 has passed. Reason for this is that sometimes the settings in the control software had to be adjusted or the HV-module was not switched on during the first seconds of a measurement, making a restart of the recording necessary. These are some of the reasons for slightly different onset times t_0.
The uncertainty of the actual temperature T_{Furnace} inside of the tube furnace is not stated in any manual so the 5% uncertainty is a rough estimation of the fluctuation of the temperature.
$\Delta d_p = 15\%$ is due to the fact that $\beta = 15\%$, which is also the uncertainty of a particle diameter reaching the DMA outlet.

5 Results

The behavior of the particle concentration right after the PET pellets got put in the tube furnace can be seen in Figure 18. The onset time t_0 was chosen to be 60 minutes since the goal was to have a concentration that was as stable as possible without t_0 being exorbitantly long.

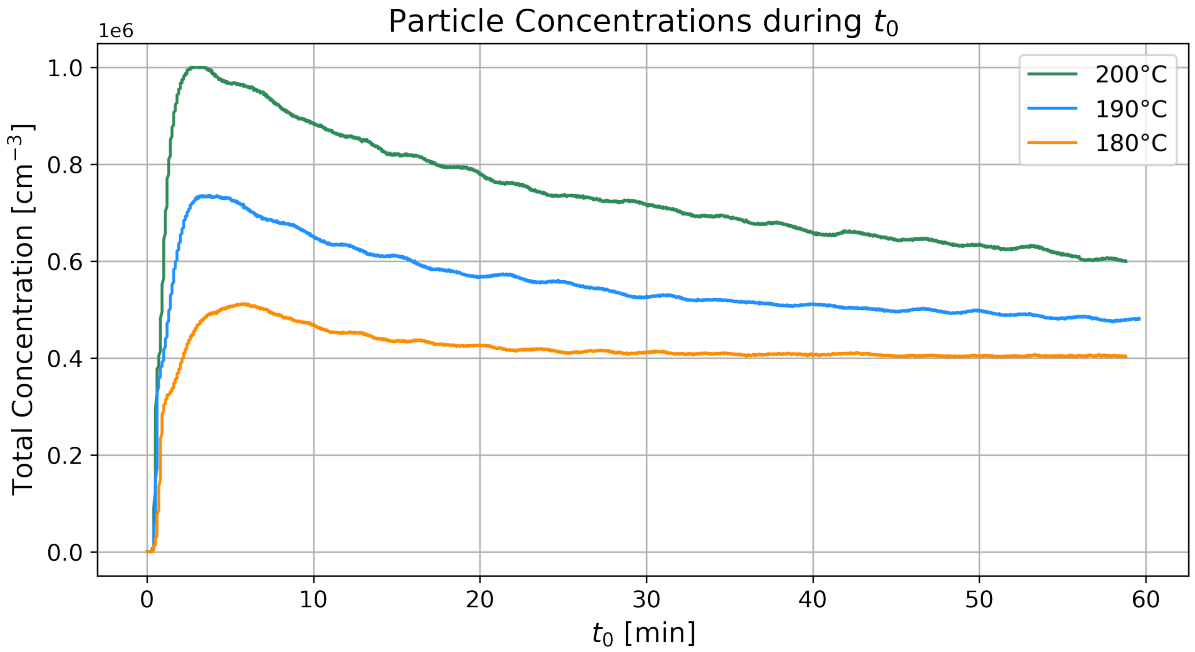

Figure 18: Particle concentrations from evaporated PET until t_0 has been reached for all 3 temperatures, measured with the TSI 3776 ($Q_F = 1.0$ lpm, $Q_D = 1.3$ lpm)

The curves seen in Figure 18 were recorded with the TSI 3776. Similar measurements with the TSI 3788 and other flows were foregone, since it would have potentially overworked the CPCs when measuring concentrations over 10^5 p/cm^3 for an hour for all 18 measurements.

Interestingly, the maximum concentration is reached in a matter of a few minutes and then starts to decline albeit way slower than the prior increase.

It is apparent that the initial surge in concentration is very similar for all temperatures. However, the peak and the eventually stabilized concentrations are increasing with the temperature, which is in unison with the expectations and the following results.

After waiting for t_0 to pass, the EMS and the HV-module were started and the recording of the number size distributions began. For every measurement 3 EMS runs were made, resulting in a recording time of approximately 40 minutes for every constellation.

In total, 18 measurements were made: 3 different flow constellations for each of the 3 temperatures and with both CPCs.

Since it wasn't clear right from the beginning if cutoff measurements were possible, meaning that a sufficiently high concentration ($> 10^3$ p/cm^3) at low diameters ($d_p \approx 2.5$ nm)

could be detected, the first measurements made were the ones for the number size distributions (NSDs).

The reason for this diameter for the cutoff measurements is that in the manual of both CPCs, the cutoff diameter was specified as $d_{p,50} = 2.5$ nm (for sucrose particles) [78] [80].

5.1 Number Size Distributions

All 18 measurements for the particle number size distributions can be seen in Figure 19, Figure 20 and Figure 21. The purple curves represent the concentrations measured with the TSI 3776 and the blue curves represent the concentrations measured with the TSI 3788. For every temperature, all 3 EMS runs are represented in the same plot.

In order to improve readability of the following figures, the error bars for the concentration and the diameters are not plotted. An estimation of the respective uncertainties can be seen in Table 5.

5.1.1 Flow 1: $Q_F = 0.8$ lpm, $Q_D = 1.5$ lpm

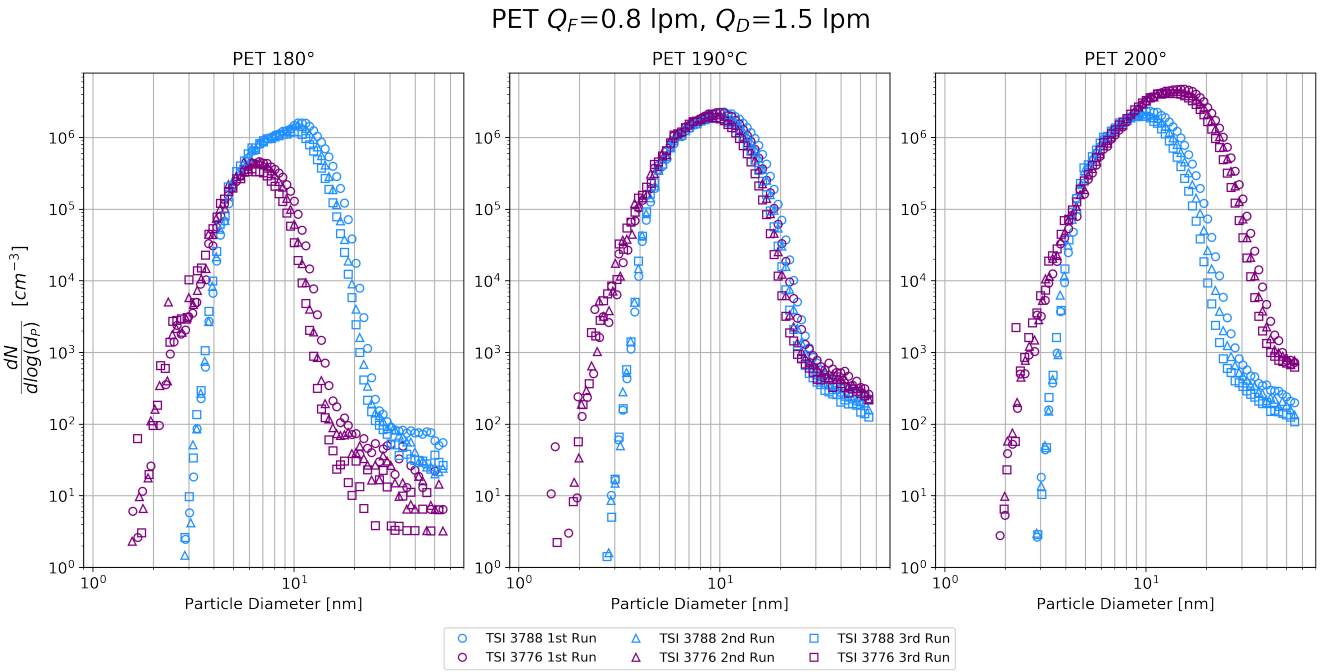

Figure 19: Number size distributions for all temperatures at $Q_F = 0.8$ lpm, Q_D=1.5 lpm

Table 6: Maximum concentrations and according mode diameters $d_{p,m}$ measured with the TSI 3788 for each temperature and run, $Q_F = 0.8$ lpm, $Q_D = 1.5$ lpm. The maximum concentrations are the calculated concentrations $dN/d\log(d_p)$.

TSI 3788	1st Run		2nd Run		3rd Run	
	$d_{p,m}$ [nm]	max. [cm^{-3}]	$d_{p,m}$ [nm]	max. [cm^{-3}]	$d_{p,m}$ [nm]	max. [cm^{-3}]
180°C	10.48	$1.60 \cdot 10^6$	10.48	$1.51 \cdot 10^6$	10.03	$1.22 \cdot 10^6$
190°C	10.48	$2.26 \cdot 10^6$	10.03	$2.09 \cdot 10^6$	9.61	$1.88 \cdot 10^6$
200°C	10.03	$2.36 \cdot 10^6$	9.61	$2.13 \cdot 10^6$	9.61	$1.99 \cdot 10^6$

Table 7: Maximum concentrations and according mode diameters $d_{p,m}$ measured with the TSI 3776 for each temperature and run, $Q_F = 0.8$ lpm, $Q_D = 1.5$ lpm. The maximum concentrations are the calculated concentrations $dN/d\log(d_p)$.

TSI 3776	1st Run		2nd Run		3rd Run	
	$d_{p,m}$ [nm]	max. [cm^{-3}]	$d_{p,m}$ [nm]	max. [cm^{-3}]	$d_{p,m}$ [nm]	max. [cm^{-3}]
180°C	6.73	$4.62 \cdot 10^5$	5.63	$4.58 \cdot 10^5$	6.17	$3.68 \cdot 10^5$
190°C	10.03	$2.26 \cdot 10^6$	9.61	$2.09 \cdot 10^6$	8.79	$1.96 \cdot 10^6$
200°C	14.93	$4.75 \cdot 10^6$	14.28	$4.42 \cdot 10^6$	13.07	$4.12 \cdot 10^6$

When comparing the graphs in Figure 19, it is noticeable that the concentrations measured with the TSI 3788 (blue graphs) seem to be rather constant for all runs and temperatures. This is further emphasized in Table 6, where not only the maximum concentrations but also the according mode diameters $d_{p,m}$, which is the diameter with the maximum concentration, do not change significantly with the temperature and run.

The opposite can be stated for the concentrations measured with the TSI 3776 (purple graphs). In this case, the maximum concentrations and the mode diameters increase with every temperature. This can be seen in Table 7.

For the TSI 3776, the mode diameters $d_{p,m}$ even double or triple from 180°C to 200°C. Another thing that stands out is that the spike, which is the point where the concentration starts to increase, starts at smaller diameters when measured with the TSI 3776, compared to the TSI 3788. This implies that smaller particles are measured at a higher concentration with the TSI 3776.

Furthermore, one can see the broadening of the curves measured with the TSI 3776 with increasing temperatures. This implies that higher concentrations are measured at every diameter.

5.1.2 Flow 2: $Q_F = 1.0$ lpm, $Q_D = 1.3$ lpm

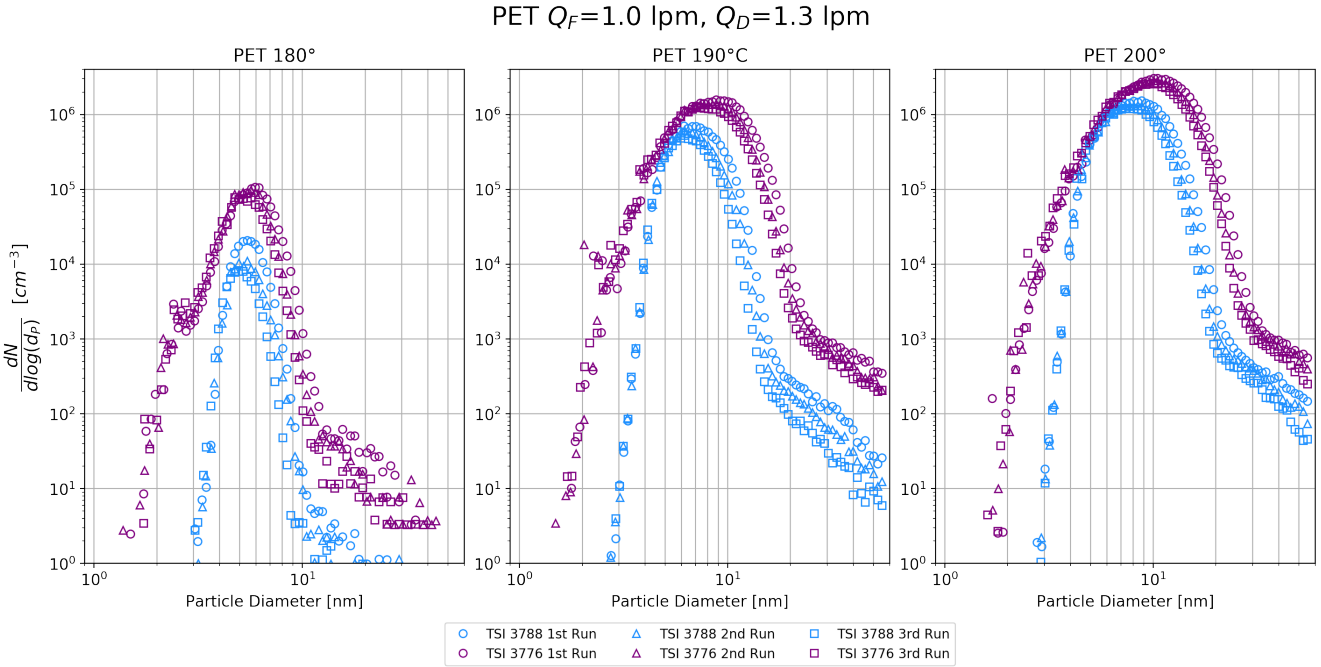

Figure 20: Number size distributions for all temperatures at $Q_F = 1.0$ lpm, Q_D=1.3 lpm

Table 8: Maximum concentrations and according mode diameters $d_{p,m}$ measured with the TSI 3788 for each temperature and run, $Q_F = 1.0$ lpm, $Q_D = 1.3$ lpm. The maximum concentrations are the calculated concentrations $dN/d\log(d_p)$.

TSI 3788	1st Run		2nd Run		3rd Run	
	$d_{p,m}$ [nm]	max. [cm^{-3}]	$d_{p,m}$ [nm]	max. [cm^{-3}]	$d_{p,m}$ [nm]	max. [cm^{-3}]
180°C	5.42	$2.07 \cdot 10^4$	5.42	$1.11 \cdot 10^4$	5.17	$8.10 \cdot 10^3$
190°C	6.16	$7.03 \cdot 10^5$	6.17	$6.16 \cdot 10^5$	6.17	$5.30 \cdot 10^5$
200°C	8.79	$1.53 \cdot 10^6$	7.35	$1.32 \cdot 10^6$	7.35	$1.22 \cdot 10^6$

For this flow constellation, it is obvious that the concentrations are lower at every diameter than with the flow constellation from section 5.1.1 ($Q_F = 0.8$ lpm, $Q_D = 1.5$ lpm).

Here, the maximum concentrations and the mode diameters increase with the temperature

Table 9: Maximum concentrations and according mode diameters $d_{p,m}$ measured with the TSI 3776 for each temperature and run, Q_F = 1.0 lpm, Q_D = 1.3 lpm. The maximum concentrations are the calculated concentrations $dN/d\log(d_p)$.

TSI 3776	1st Run		2nd Run		3rd Run	
	$d_{p,m}$ [nm]	max. [cm^{-3}]	$d_{p,m}$ [nm]	max. [cm^{-3}]	$d_{p,m}$ [nm]	max. [cm^{-3}]
180°C	5.92	$1.08 \cdot 10^5$	5.67	$9.78 \cdot 10^4$	4.72	$7.84 \cdot 10^4$
190°C	8.79	$1.57 \cdot 10^6$	8.79	$1.40 \cdot 10^6$	7.35	$1.25 \cdot 10^6$
200°C	10.03	$3.07 \cdot 10^6$	10.03	$2.86 \cdot 10^6$	10.03	$2.65 \cdot 10^6$

for both the TSI 3788 and TSI 3776. This can also be seen in Table 8 and Table 9.

However, the maxima and respective mode diameters are bigger at every temperature when measured with the TSI 3776. Also, the increase of $d_{p,m}$ with the temperature is higher when measured with the TSI 3776.

In addition to that, the spike of the curves start at smaller diameters when measured with the TSI 3776, which is in agreement with the results from section 5.1.1.

Furthermore, a broadening of the curves when increasing the temperature can be seen as well, this time for both CPCs in similar fashion.

In general, it can be stated that the blue curves measured with the TSI 3788 lay within the purple curves measured with the TSI 3776, which means that the TSI 3776 detects a higher concentration than the TSI 3788 at every particle diameter.

5.1.3 Flow 3: Q_F = 1.2 lpm, Q_D = 1.1 lpm

Table 10: Maximum concentrations and according mode diameters $d_{p,m}$ measured with the TSI 3788 for each temperature and run, Q_F = 1.2 lpm, Q_D = 1.1 lpm. The maximum concentrations are the calculated concentrations $dN/d\log(d_p)$.

TSI 3788	1st Run		2nd Run		3rd Run	
	$d_{p,m}$ [nm]	max. [cm^{-3}]	$d_{p,m}$ [nm]	max. [cm^{-3}]	$d_{p,m}$ [nm]	max. [cm^{-3}]
180°C	6.16	$5.56 \cdot 10^4$	5.67	$4.80 \cdot 10^4$	5.67	$3.99 \cdot 10^4$
190°C	5.67	$4.75 \cdot 10^4$	5.17	$3.18 \cdot 10^4$	5.41	$2.37 \cdot 10^4$
200°C	8.79	$4.61 \cdot 10^5$	8.41	$4.25 \cdot 10^5$	8.04	$3.69 \cdot 10^5$

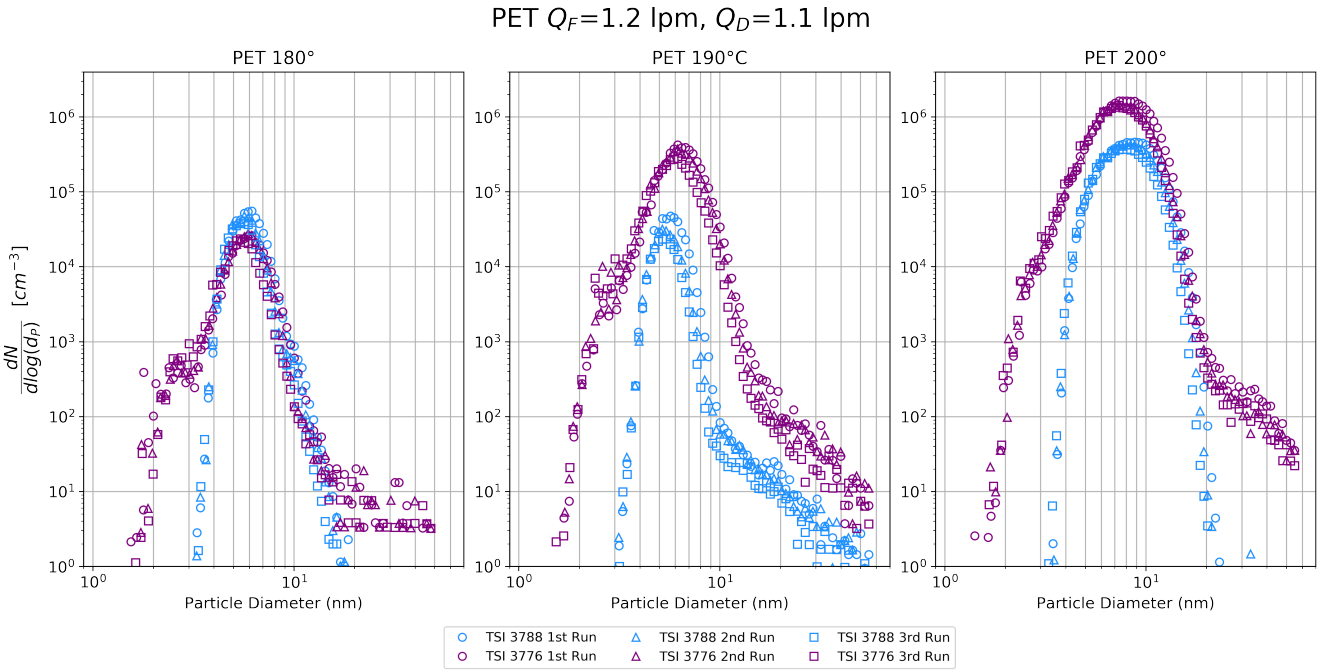

Figure 21: Number size distributions for all temperatures at $Q_F = 1.2$ lpm, Q_D=1.1 lpm

Table 11: Maximum concentrations and according mode diameters $d_{p,m}$ measured with the TSI 3776 for each temperature and run, $Q_F = 1.2$ lpm, $Q_D = 1.1$ lpm. The maximum concentrations are the calculated concentrations $dN/d\log(d_p)$.

TSI 3776	1st Run		2nd Run		3rd Run	
	$d_{p,m}$ [nm]	max. [cm^{-3}]	$d_{p,m}$ [nm]	max. [cm^{-3}]	$d_{p,m}$ [nm]	max. [cm^{-3}]
180°C	6.17	$2.59 \cdot 10^4$	5.92	$2.77 \cdot 10^4$	5.41	$2.35 \cdot 10^4$
190°C	6.17	$4.22 \cdot 10^5$	6.17	$3.74 \cdot 10^5$	6.17	$2.79 \cdot 10^5$
200°C	7.35	$1.63 \cdot 10^6$	7.35	$1.47 \cdot 10^6$	7.35	$1.42 \cdot 10^6$

At this flow, it is further observable that the concentrations decrease at every point when comparing them to the results for lower Q_F's (s. section 5.1.1 and section 5.1.2).

Unsurprisingly, the concentrations increase at every diameter when increasing the temperature, which is also in agreement with the prior results.

The TSI 3776 measures a higher concentration at every diameter, resulting in a spike at smaller diameters with the TSI 3776.

Sole exception is the left graph in Figure 21 (180°C). Nonetheless, the concentration peak for both CPCs at 180°C are equal within the uncertainties, yet the spike also starts at

lower d_p's with the TSI 3776.

Like in section 5.1.2, the blue curves measured with the TSI 3788 are within the purple curves measured with the TSI 3776 in most cases, further emphasizing that the TSI 3776 measures higher concentrations at every diameter.

5.1.4 Discussion of Number Size Distribution Results

When comparing the graphs, it is clear that with increasing temperature, the concentration gets higher at every diameter. This matches with the expectations prior to the measurements.

A likely explanation is that the higher the temperature is the faster the PET evaporates resulting in a higher production of particles.

That effect is visible in every plot. However, it is not constant for every flow constellation. The lower the initial concentration at the lowest temperature 180°C is, the more the particle concentration increases with the temperature.

Another factor when it comes to the particle concentration is the flow Q_F through the furnace. Although it might not be initially obvious, the lower the Q_F's, the higher the concentration gets. When comparing the lowest $Q_F = 0.8$ lpm (Figure 19) with the highest $Q_F = 1.2$ lpm (Figure 21), it is apparent that the concentration is higher at every diameter when $Q_F = 0.8$ lpm. A possible explanation for that is since the aerosol flow has a higher velocity at $Q_F = 1.2$ lpm, it cannot reach the set temperature due to the cooling effect on the aerosol.

This cooling effect is further emphasized by the broadening of the curves. The higher the temperatures and the lower the flow Q_F, the broader the curves are.

Hence, the broadest curves for each flow constellation are visible at the maximum temperatures of 200°C and the lowest $Q_F = 0.8$ lpm (Figure 19).

The dilution flow Q_D was chosen in order to get the respective flows to 2.3 lpm in total to get a DMA resolution $\beta = 15\%$. During the measurements it was quickly found out that a rather big change of Q_D did not change the measured concentration significantly.

Interestingly, a decrease in Q_D leads to a decrease in particle concentration. This effect, however, originates primarily from the increase in Q_F and the resulting decrease in dilution Q_D.

In addition to that, it is observable that the higher the total particle concentrations become, the larger the mode diameters $d_{p,m}$ become. The results of the mode diameters can be seen in the respective tables from the prior results.
However, a relatively significant particle growth due to coagulation during a single measurement was only observed at $Q_F = 0.8$ lpm, 200°C and when measured with the TSI 3776 - the constellation of flows and temperature that yielded the highest total particle concentration.
Assuming that the total length of tubing was about 1 m with a tube diameter of 0.56 cm, the aerosol took about 1.79 seconds at a flow of $Q_F = 0.8$ lpm and about 1.43 seconds at a flow of $Q_F = 1.0$ lpm to get from the furnace to the DMA.
In only three measurements the coagulation had a noticeable influence on the total measured concentration and on the mode diameter $d_{p,m}$. All of these measurements were made with the TSI 3776. The results can be seen in Table 12:

Table 12: Measurements where the effect of coagulation was noticeable. The total particle concentrations N_0 and $N(t)$ are the sum of the concentrations in all 97 channels and are the calculated concentrations $dN/d\log(d_p)$.

Q_F [lpm]	Temp. [°C]	N_0 [cm^{-3}]	$N(t)$ [cm^{-3}]	d_0 [nm]	$d(t)$ [nm]
0.8	200	$1.16 \cdot 10^8$	$9.7 \cdot 10^7$	14.06	14.93
0.8	190	$4.36 \cdot 10^7$	$4.06 \cdot 10^7$	9.79	10.03
1.0	200	$6.57 \cdot 10^7$	$6.03 \cdot 10^7$	9.74	10.03

The results were calculated using Equation 16 and Equation 17.
Unsurprisingly, these 3 measurements are also the ones with the highest total concentration and the highest mode diameters.
With all other measurements, the change in particle size and total concentration was not significant and was within the uncertainties, mostly because the total concentration was

not as high as in the aforementioned constellations and the mode diameters $d_{p,m}$ were smaller, which are two of the most important parameters for coagulation. Furthermore, at higher flows the time the aerosol takes to get from the furnace to the DMA decreased, so in addition to the already lower produced particle concentration and smaller produced particles, the time in which coagulation could occur decreased, making coagulation even less likely.
Therefore, one can assume that coagulation is not the reason why the mode diameters $d_{p,m}$ grow with the temperature in the furnace. A more likely reason is simply that by increasing the temperature in the furnace and decreasing the flow Q_F, larger particles are produced in higher concentration. These particles eventually grow slightly by coagulation, but this effect cannot explain these vast increases in diameter.

In general, with the TSI 3776 one can observe a higher concentration for lower particles, the concentration peak is higher and larger particles are also measured in higher concentrations. Sole exception for this seems to be at $Q_F = 0.8$ lpm, $Q_D = 1.5$ lpm and 180 °C (Figure 19, left plot), where larger particles are measured in a higher concentration with the TSI 3788. However, smaller particles ($d_p \leq 4$ nm) are still better detected with the TSI 3776, which is in agreement with all the other measurements.
This leads to the conclusion that PET particles are activated and measured better with the TSI 3776 having butanol as the working fluid.

Another plot that is not consistent with the others is $Q_F = 1.2$ lpm, $Q_D = 1.1$ lpm and 180°C (Figure 21, left plot), where the TSI 3788 measures a slightly higher concentration around the peak at $d_p \approx 6$ nm than the TSI 3776. However, the two curves match each other within the uncertainties of the respective CPCs. Yet again, smaller particles are detected better with the butanol CPC.
Contrary to the other results the maximum concentration is slightly declining when raising the temperature from 180 °C to 190 °C at this flow . A possible explanation could be that the PET pellets inside the spoon were in a position that did not allow them to heat

up like they could in the other measurements. It is likely that they moved around inside the spoon when inserted into the tube furnace - an effect that was very hard to control and prevent. Furthermore the glass spoon itself could have been in a position that was slightly outside the heating zone, consequently the pellets could not heat up as desired. Another likely explanation is that the pellets varied in mass, resulting in a lower particle concentration.
However, this irregularity is rather small and can only be observed once out of all the measurements.

Furthermore, it is also visible that the maximum concentration is the highest in every single 1st run and decreases in the following runs. This is also in agreement with Figure 18 and Figure 22, where one can see that the total concentration and the maximum decrease with time, respectively. The decrease seems to be constant for all temperatures and flows. This is further proven by the mode diameters, which get smaller at every run, albeit this effect is rather small.

Looking at the total concentration in Figure 18, one can see that for the lowest temperature of T = 180°C, the concentration stabilizes rather fast compared to the highest temperature of T = 200°C. In the latter case, the concentration seems to stabilize at some point after t_0 = 60 minutes. This becomes very interesting when comparing it with the particle number size distributions. There, the concentration of particles in the upper end of the measured spectrum seem to be less stable at the lowest temperature of 180°C.
This can be explained by the signal to noise ratio. The higher the measured concentration is, the higher the signal to noise ratio becomes, eliminating the impact of any "noise" particles the CPC might measure. Since the concentration of large particles has a lower magnitude at lower temperatures, this ratio becomes small and alters the measurements, resulting in a higher fluctuation of measured concentrations at this end of the diameter spectrum.

5.2 Decline of total concentration

In order to further investigate the decline of produced particles, 16 EMS runs were recorded with flows of Q_D = 1.0 lpm and Q_F = 1.3 lpm and at a temperature of 190°C. The aim of this measurement was to check whether there was a time when the concentration would become constant and stabilize and when that time would arrive. The result can be seen in Figure 22.

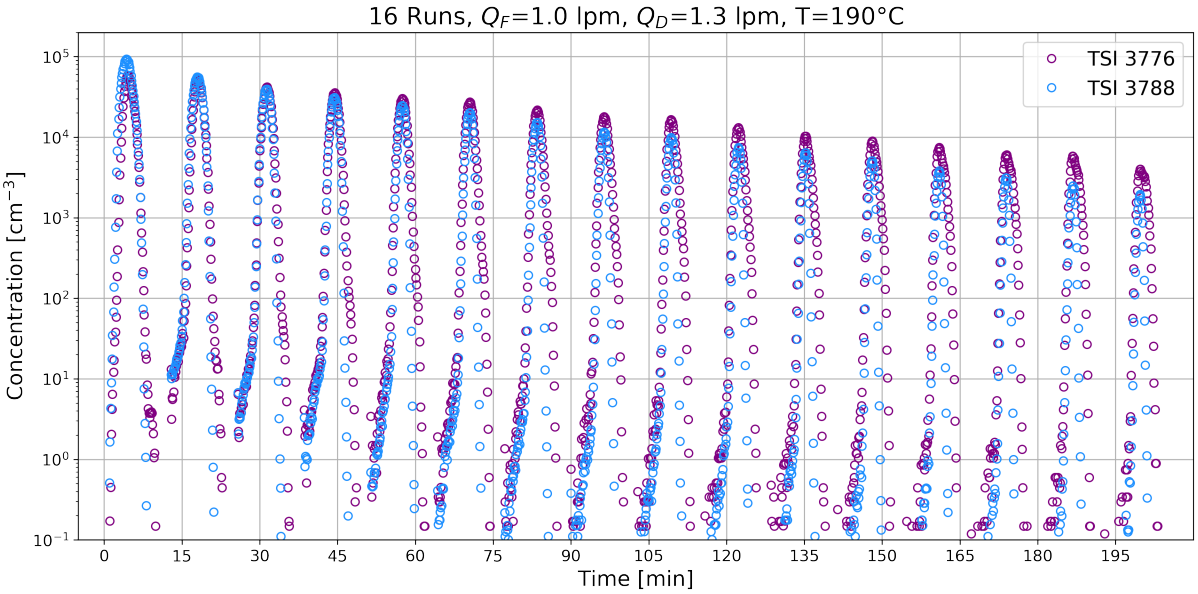

Figure 22: Recording of 16 Runs at a temperature of 190 °C, Q_F=1.0 lpm, Q_D=1.3 lpm with both the TSI 3776 and the TSI 3788

In total, the sample was in the tube furnace for 200 minutes. It is apparent that the peak of the concentrations didn't stabilize and the decline of the peaks continued during the recording time of 200 minutes.

Therefore, there is reason to believe that there is no point in time when the peak concentrations become constant run for run and if there is, it would extend the necessary measurements exorbitantly long.

Additionally, it is observable that with the exception of the first 2 runs, the TSI 3776 measures higher concentrations. This is also in agreement with the results above.

A possible reason why the first two runs show a higher concentration when measured with the TSI 3788 is because the PET pellets had different positions in the spoon and in the

tube furnace, they could take on the temperature of the furnace quicker, resulting in an initially higher particle production when measured with the TSI 3788. Also, the used PET pellets likely differed slightly in mass, which could also have an effect on the initial particle production.

It should be noted that the recording of the concentrations began right away and the onset time $t_0 = 60$ min was not waited out.

These results further point out the importance of a certain onset time in which the particles heat up in the tube furnace prior to the actual recordings. It makes the measurements more reproducible, as the particle production stabilizes and uncontrollable factors such as exact pellet placements can be constrained.

5.3 Cutoff Diameters

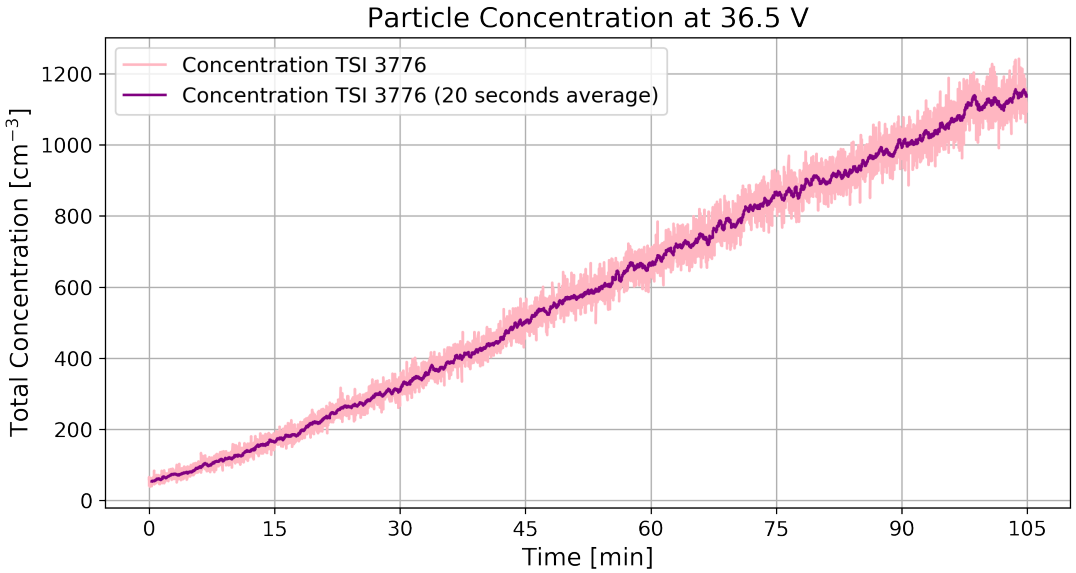

Figure 23: PET Particle Concentration at a DMA voltage of 36.5 V $\approxeq$ 2.5 nm over a time frame of 105 minutes, measured with the TSI 3776. The onset time t_0 was not awaited and recording began right after the pellets were inserted into the furnace.

Interestingly, even though the total concentration and the maxima decline with time (Figure 18, Figure 22), the concentration of smaller particles seem to increase in the same time frame. In Figure 23, it is observable that the concentration of particles with $d_p \approx 2.5$ nm increase from 0 to over 10^3 within 105 minutes. This measurement was achieved by setting the HV-module connected to the DMA to 36.5 V which corresponds to approximately 2.5 nm. An exact calculation and setting of the correct voltage equal to 2.5 nm was foregone, since this measurement was just to get a general overview of how particles with diameters in the magnitude of where $d_{p,50}$ could be expected, behave with time.
This increase in particles made cutoff measurements possible, since a concentration of at least 10^3 p/cm^3 in the vicinity of 2.5 nm had to be achieved in order to minimize the signal to noise ratio of the devices, especially of the FCE, and get satisfying results.

Since both CPS and the FCE have an inlet flow of about 1.5 lpm, changes in the flows had to be made in order to get Q_a over the necessary 3 lpm. However, the DMA resolution still had to remain $\beta = 0.15$. This was achieved by increasing the dilution flow Q_D by 1

lpm for every constellation and changing the critical orifice of the DMA to get a new flow for both Q_{sh} and Q_{ex}.

The cutoff measurements were made with only one constellation of temperature and flows. This constellation was chosen based on the obtained results from the number size distributions in section 5.1, where the most particles of smaller diameters were measured. The constellation of flow and temperature for the cutoff measurements can be seen in Table 13.

Table 13: Flows and Temperature for the cutoff measurements

Temperature	(200 ± 5) °C
Q_F	(1.0 ± 0.1) lpm
Q_D	(2.3 ± 0.1) lpm
Q_A	(3.3 ± 0.4) lpm
Q_{sh}	(21.8 ± 0.4) lpm
Q_{ex}	(21.7 ± 0.4) lpm

In principle, the process and the preparations prior to the actual measurements were similar to the measurements for the number size distribution.

The only differences were that the monodisperse aerosol flow from the DMA was now split into two different measurement devices instead of only one CPC and the resulting new flows. The new setup can be seen in Figure 24:

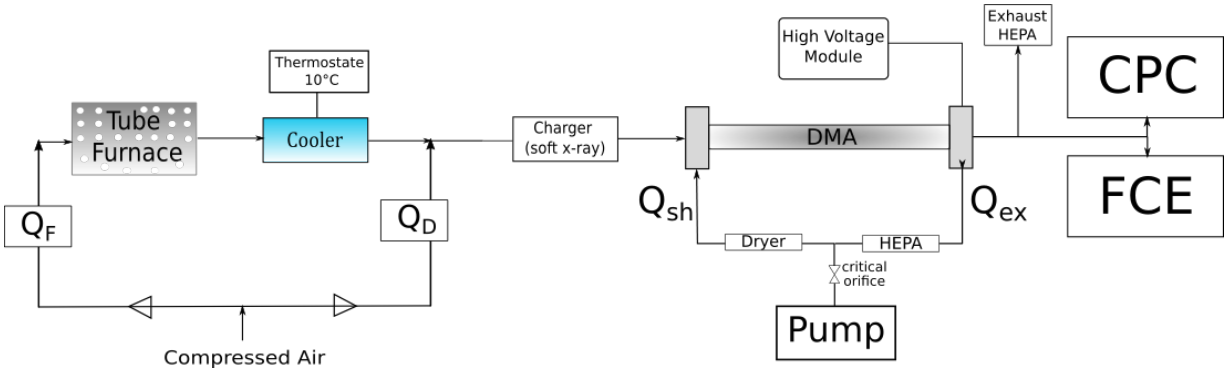

Figure 24: Schematic of the cutoff measurements. The working principle is the same as in Figure 16, except the aerosol is split into the CPC and the FCE that measure the concentration of size selected particles simultaneously

5.3.1 Results of the Cutoff Measurements

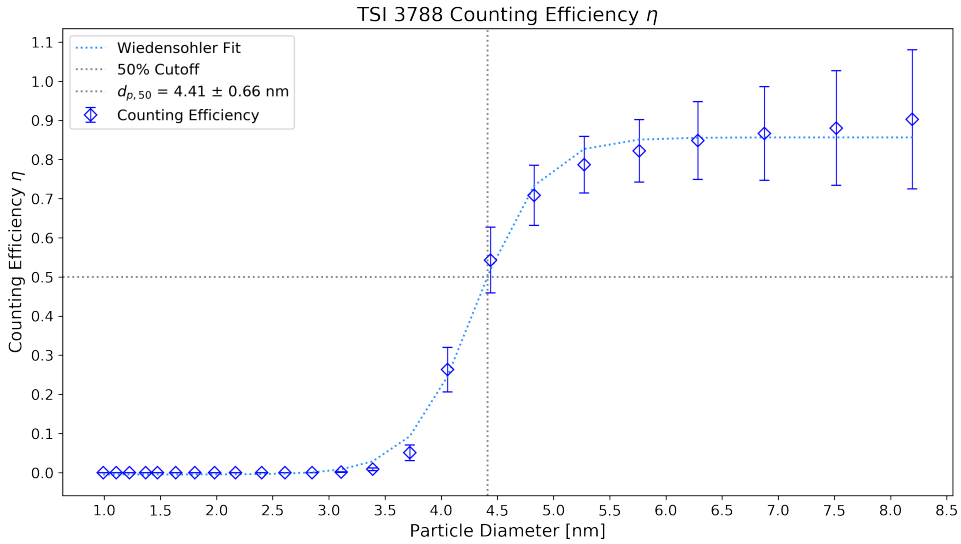

Figure 25: Counting efficiency curve measured with the TSI 3788. The data was fit with the Wiedensohler fit function

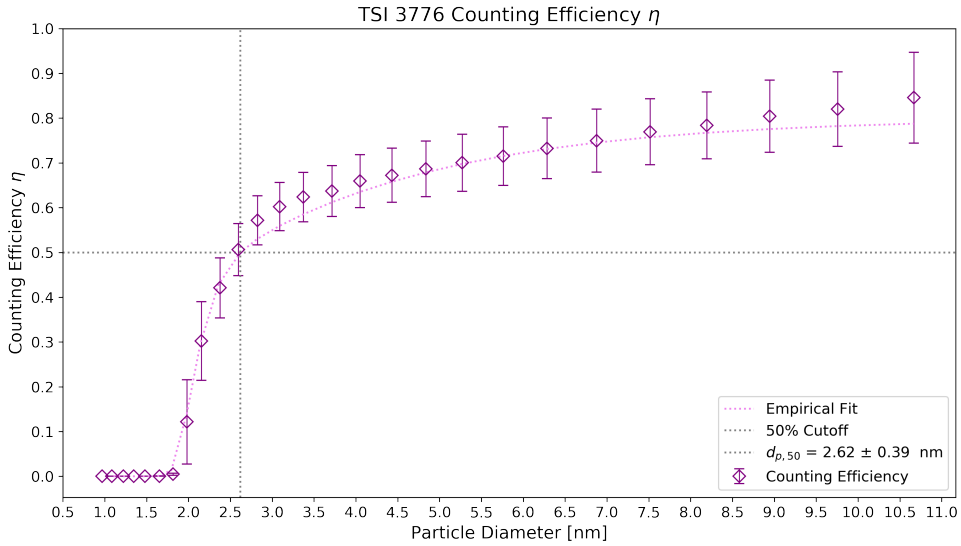

Figure 26: Counting efficiency curve measured with the TSI 3776. The data was fit with an empirical fit function

Table 14: Cutoff Diameters $d_{p,50}$ and uncertainty $\Delta d_{p,50}$ for both CPCs

CPC	$d_{p,50}$	$\Delta d_{p,50}$
TSI 3788	4.41 nm	0.66 nm
TSI 3776	2.62 nm	0.39 nm

The data was fit with the Wiedensohler Fit function [91] for the TSI 3788 and an empirical fit function [69] for the TSI 3776.

Wiedensohler fit function:

$$y = \frac{a - b}{1 + \exp\left(\frac{x - x_1}{x_2}\right)} \tag{42}$$

Empirical fit function:

$$y = a \cdot e^{-\exp(-k(x - x_0))} \cdot \left(1 - e^{-x \cdot n}\right) \tag{43}$$

with the following parameters:

Table 15: Parameters of the empirical fit function [69]

Parameter	Definition	Value
a	Position of Plateu	0.8
k	Curvature	6
x_0	Offset	2
n	nth root function	0.39

The parameters were chosen by trying different values and seeing what values fit the curve the best.

The reason why two different fit functions were used was that the Wiedensohler fit did not match the data for the TSI 3766. However, for the TSI 3788, the fit matched the data very good.

The uncertainty of the cutoff diameter was set as 15%. The reason for this can be seen in Equation 36.

The resulting error bars of the diameters d_p in Figure 25 and Figure 26 were not plotted to increase visibility since ± 15% is the uncertainty for every single diameter.

5.3.2 Discussion of Cutoff Measurements

Figure 23 clearly shows that the longer the pellets are in the tube furnace, the smaller the produced particles become.

This proves that the longer the pellets are heated, the more they degrade into smaller and smaller pieces.
This is not initially obvious, since the total concentration decreases, which could lead to the assumption that the particles become bigger due to i.e. coagulation.
A possible explanation might be that they eventually degrade into particles with such a small diameter ($d_p < 2$ nm) that they might not be able to be detected by the CPC.

When comparing the two counting efficiency curves measured with the TSI 3788 (Figure 25) and the TSI 3776 (Figure 26) it becomes immediately clear that smaller particles are detected better with the TSI 3776. This is further emphasized by the 50% - cutoff diameters $d_{p,50}$ as seen in Table 14.
Consequently, PET particles are activated better when measured with butanol CPCs. This is also in agreement with the results from section 5.1, which show that the TSI 3776 detected a higher concentration at almost any particle diameter, especially lower diameters, than the TSI 3788, independently of the flows and temperature.
The lower cutoff diameter measured with the TSI 3776 is another proof of what was stated in section 3.11.1 and is also in agreement with Wlasits et.al [85]. The presented results show that the rather nonpolar PET seed particles interact better with butanol, a rather nonpolar fluid than with water, a highly polar fluid.

Another thing that stands out is the plateau of the curves at higher diameters. Ideally, the counting efficiency should increase for particles with $d_p > d_{p,50}$ until it reaches a plateau of 1, meaning an efficiency of 100%. This is not the case for both curves. Here, the plateau is around 0.8 for the TSI 3788 and around 0.75 for the TSI 3776.
A possible explanation for the plateau being below 1 is particle diffusion, as explained in section 3.5. Since the tube length inside of the CPCs are longer (approx. 28.5 cm) than the distance the particles travel inside the FCE, these tubes are a source of diffusion on to its tube walls. This effect results in an inevitable loss of particles right before their detection, possibly explaining the discrepancy of 20% and 25% in maximum detection

efficiency, respectively.

The tube length of a TSI 3788 was determined by unscrewing an old defunct model and estimating the length. Since no defunct TSI 3776 was available, the tube was assumed to be as long as in the TSI 3788.

Of course, this estimation was a vague way of determining the tube length, but unfortunately, a more precise way was not feasible. Additionally, in the manual of either CPC the length of the tubes was not noted.

A determination of said distance in the FCE could not be done because unscrewing and opening this device was deemed too risky and no defunct model was available.

In addition to that, the inlet flow of the TSI 3788 is marginally higher than the one of the TSI 3776, which might explain why the plateau of the TSI 3788 is slightly higher than the plateau of the TSI 3776. The inlet flows Q_{in} can be seen in Table 16.

Table 16: Inlet flows Q_{in} of the devices used in the experiments

Device	Q_{in} [lpm]	ΔQ_{in} [lpm]
TSI 3788	1.57	0.02
TSI 3776	1.43	0.01
FCE	1.50	0.01

The flow rates Q_{in} were measured with the *Gilibrator - 2* flowmeter. For every Q_{in} a series of 10 measurements were made and the error was determined by propagation of uncertainty.

Since these flow rates are fixed for all devices and cannot be adjusted manually in small steps, these minor discrepancies in the flow could not be changed.

Interestingly, the PET counting efficiency curve measured with the TSI 3776 (s. Figure 26) and the counting efficiency curves for different materials measured by Wlasits et. al. ([69]) share some similarities.

The curves for $C_{15}H_{24}O_X$, $(NH_4)_2SO_4$ and Ag all have similar shapes compared to PET.

The counting efficiency increases rather fast at smaller diameters but a plateu seems to be reached rather slow and never stabilizes at a value of around 1 in both cases, even after the upper limit of measurement at 10 nm and 11 nm, respectively.
Additionally, the cutoff-diameters for all aforementioned materials have comparable values (s. Table 17) and lay within their respective uncertainties. Therefore, the counting efficiency curve and the cutoff-diameter of the TSI 3776 when measuring PET have been found for other materials in a resembling form .

Table 17: TSI 3776 cutoff-diameters $d_{p,50}$ for different materials according to Wlasits et. al. [69]

Material	$d_{p,50}$ [nm]	$\Delta d_{p,50}$ [nm]
$C_{15}H_{24}O_X$	2.8	0.3
$(NH_4)_2SO_4$	3.1	0.4
Ag	3.0	0.3
PET	2.6	0.4

5.4 Aftermath of a measurement

Figure 27: PET pellets prior and after a measurement

In Figure 27 the comparison of unused and used pellets after a measurement is observable. This particular picture was made after a measurement at 200°C and flows of $Q_F = 0.8$ lpm, $Q_D = 1.5$ lpm.

Unsurprisingly, the pellets have not melted. They have gotten a bit of a brownish hue, however. This hue arose in all measurements, regardless of temperature and flow.
The pellets did not stick into the spoon after any measurement and fell out at the slightest push.
Nonetheless, there seemed to be some rest particles not visible to the eye that remained in the spoon, since the empty spoon produced particles after put back into the tube furnace. In order to prevent these rest particles to interfere with the upcoming measurements, the spoon was heated out in the furnace by setting the temperature to 350°C and leaving the spoon in for about 20 minutes. When the furnace has cooled off to the desired temperature for the next measurements, the concentration was measured again and if the CPC detected no particles, new pellets were inserted and new measurements began.

6 Conclusion

This experiment was one of the first to produce nanoplastic particles that originate from larger plastic pellets in a controlled laboratory environment. By alternating different parameters, namely the temperature the polymers are heated up to and the flow rates of the aerosol and by creating monodisperse aerosol with the DMA, these measurements give insight on the diameters nanoplastic can have when heated.
The produced particles have a wide range of diameters between 2 nm and 54,6 nm and the diameters are lognormal distributed with a clear visible peak in concentration.

The results demonstrate that PET is activated better when measured with the TSI 3776 with butanol as the working fluid compared to the TSI 3788 with water as the working fluid. Not only are the concentrations over the whole measured diameter spectrum higher, but the cutoff diameter $d_{p,50}$ is also significantly lower when measured with the TSI 3776. These results give insight on the polarity of PET and further prove what was stated by Wlastits et.al. (2020) [85]: Seed particles are better activated and detected when it has chemical similarities in terms of polarity with the working fluid.
Therefore, a nonpolar working fluid such as butanol should be used to measure nanoplastic particles originating from PET.
It also underlines that the cutoff diameter $d_{p,50}$ has to be measured individually for every material and every CPC in a controlled environment.
It is demonstrated that nanoplastics coming from PET are being produced far below the melting points of the polymer. This leads to the conclusion that PET nanoparticles can emerge without melting the plastic and therefore can be produced at lower temperatures than one might assume initially.
In addition to that, a very high concentration of particles can be observed almost immediately after heating the plastic. This production of high concentrations of nanoplastics does not require a high initial mass of the heated plastic, as the mass of the PET plastic did not exceed a few percents of a gram. This could very well mean that such nanoplastic particles can be generated by anybody and anywhere, especially at home in the kitchen

for example, where temperatures as high as in these experiments occur on a daily basis.

7 Future Research

In order to further address this new and rather unexplored topic of research, it would be very interesting to see what diameters the produced particles have when the PET pellets are heated above their melting temperature. The results in this thesis show that with increasing temperature the particle concentrations also increase. However, one cannot say with 100% certainty that this effect holds for temperatures above 225°C, since these temperatures were not covered during these measurements. It is also possible that particles with a diameter way below 2 nm can be produced that way.

Of course, these high temperatures would mean that a new approach has to be found in terms of how the pellets are inserted into the tube furnace, since burning the pellets into the glass spoon is inevitable. One would have to put a protective layer in between the glass and the pellets that is easily accessible, moldable, and - most importantly - does not produce any particles that change the outcome of the measurements when heated at high temperatures.

List of Figures

List of Tables

References

1. Hinds, W. C. *Aerosol technology : properties, behavior, and measurement of airborne particles* Second edition. eng. ISBN: 9781118591970 (John Wiley Sons, Ins., New York, 1999).
2. Oberdörster, G., Oberdörster, E. & Oberdörster, J. Nanotoxicology: an emerging discipline evolving from studies of ultrafine particles. *Environmental health perspectives* **113,** 823–839 (2005).
3. Peters, A. *et al.* Translocation and potential neurological effects of fine and ultrafine particles a critical update. *Particle and fibre toxicology* **3,** 1–13 (2006).
4. Ramanathan, V. & Feng, Y. Air pollution, greenhouse gases and climate change: Global and regional perspectives. *Atmospheric Environment* **43.** Atmospheric Environment - Fifty Years of Endeavour, 37–50. ISSN: 1352-2310. https://www.sciencedirect.com/science/article/pii/S1352231008008583 (2009).
5. *Plastics - The Facts 2020* https://www.plasticseurope.org/en/resources/publications/4312-plastics-facts-2020.
6. Lambert, S. & Wagner, M. Characterisation of nanoplastics during the degradation of polystyrene. eng. *Chemosphere (Oxford)* **145,** 265–268. ISSN: 0045-6535 (2016).
7. Ekvall, M. T. *et al.* Nanoplastics formed during the mechanical breakdown of daily-use polystyrene products. *Nanoscale Advances* **1,** 1055–1061 (2019).
8. Dawson, A. L. *et al.* Turning microplastics into nanoplastics through digestive fragmentation by Antarctic krill. *Nature communications* **9,** 1001. https://uaccess.univie.ac.at/login?url=https://www-proquest-com.uaccess.univie.ac.at/scholarly-journals/turning-microplastics-into-nanoplastics-through/docview/2012916134/se-2?accountid=14682 (Mar. 2018).

9. Stokes, V. K. *Introduction to Plastics Engineering* eng. ISBN: 9781119536574 (John Wiley Sons, Incorporated, Newark, 2020).
10. Crawford, C. B. & Quinn, B. *Microplastic Pollutants* eng. ISBN: 9780128094068 (Elsevier Science Technology, Kent, 2016).
11. *PET Pellets by Sigma-Aldrich Data Sheet* https://www.sigmaaldrich.com/AT/en/product/aldrich/429252?context=product.
12. *dielectric constants on polymerdatabase.com* https://polymerdatabase.com/polymer%20physics/Epsilon%20Table.html.
13. *Resin codes - what do they mean* https://www.2ea.co.uk/Plastics--Resin-Codes-What-do-they-mean.html.
14. Lucas, J. & Adam, J.-L. in *Encyclopedia of Materials: Science and Technology* (eds Buschow, K. J. *et al.*) 3205–3209 (Elsevier, Oxford, 2001). ISBN: 978-0-08-043152-9. https://www.sciencedirect.com/science/article/pii/B0080431526005702.
15. Gigault, J. *et al.* Current opinion: What is a nanoplastic? eng. *Environmental pollution (1987)* **235,** 1030–1034. ISSN: 0269-7491 (2018).
16. *ISO/TS 80004-1:2015 Nanotechnologies* https://www.iso.org/standard/68058.html.
17. *Plastics and the Environment* eng. ISBN: 9781788013314 (Cambridge, UK : 2019).
18. Stephens, B., Azimi, P., El Orch, Z. & Ramos, T. Ultrafine particle emissions from desktop 3D printers. *Atmospheric Environment* **79,** 334–339. ISSN: 1352-2310. https://www.sciencedirect.com/science/article/pii/S1352231013005086 (2013).
19. Lusher, A., Tirelli, V., O'Connor, I. & Officer, R. Microplastics in Arctic polar waters: The first reported values of particles in surface and sub-surface samples. *Scientific Reports* **5:14974** (Nov. 2015).
20. Waller, C. L. *et al.* Microplastics in the Antarctic marine system: An emerging area of research. *Science of The Total Environment* **598,** 220–227. ISSN: 0048-9697. https://www.sciencedirect.com/science/article/pii/S0048969717308148 (2017).

21. Ling, S., Sinclair, M., Levi, C., Reeves, S. & Edgar, G. Ubiquity of microplastics in coastal seafloor sediments. *Marine Pollution Bulletin* **121,** 104–110. ISSN: 0025-326X. https://www.sciencedirect.com/science/article/pii/S0025326X17304265 (2017).

22. Ter Halle, A. *et al.* Nanoplastic in the North Atlantic Subtropical Gyre. eng. *Environmental science technology* **51,** 13689–13697. ISSN: 0013-936X (2017).

23. Barnes, D., Galgani, F., Thompson, R. & Barlaz, M. Accumulation and fragmentation of plastic debris in global environments. *Philosophical transactions of the Royal Society of London. Series B, Biological sciences* **364,** 1985–98 (Aug. 2009).

24. Anselmo, A. C. *et al.* Delivering Nanoparticles to Lungs while Avoiding Liver and Spleen through Adsorption on Red Blood Cells. eng. *ACS nano* **7,** 11129–11137. ISSN: 1936-0851 (2013).

25. Chambers, E. & Mitragotri, S. Prolonged circulation of large polymeric nanoparticles by non-covalent adsorption on erythrocytes. eng. *Journal of controlled release* **100,** 111–119. ISSN: 0168-3659 (2004).

26. Yang, C.-S. *et al.* Nanoparticle-Based in Vivo Investigation on Blood−Brain Barrier Permeability Following Ischemia and Reperfusion. eng. *Analytical chemistry (Washington)* **76,** 4465–4471. ISSN: 0003-2700 (2004).

27. Rafiee, M. *et al.* Neurobehavioral assessment of rats exposed to pristine polystyrene nanoplastics upon oral exposure. eng. *Chemosphere (Oxford)* **193,** 745–753. ISSN: 0045-6535 (2018).

28. Lehner, R., Weder, C., Petri-Fink, A. & Rothen-Rutishauser, B. Emergence of Nanoplastic in the Environment and Possible Impact on Human Health. *Environmental Science & Technology* **53.** PMID: 30629421, 1748–1765. https://doi.org/10.1021/acs.est.8b05512 (2019).

29. Li, J., Yang, D., Li, L., Jabeen, K. & Shi, H. Microplastics in commercial bivalves from China. eng. *Environmental pollution (1987)* **207,** 190–195. ISSN: 0269-7491 (2015).

30. Neves, D., Sobral, P., Ferreira, J. L. & Pereira, T. Ingestion of microplastics by commercial fish off the Portuguese coast. *Marine Pollution Bulletin* **101,** 119–126. ISSN: 0025-326X. https://www.sciencedirect.com/science/article/pii/S0025326X15301582 (2015).

31. Devriese, L. I. *et al.* Microplastic contamination in brown shrimp (Crangon crangon, Linnaeus 1758) from coastal waters of the Southern North Sea and Channel area. *Marine Pollution Bulletin* **98,** 179–187. ISSN: 0025-326X. https://www.sciencedirect.com/science/article/pii/S0025326X1500418X (2015).

32. Yang, D. *et al.* Microplastic Pollution in Table Salts from China. eng. *Environmental science technology* **49,** 13622–13627. ISSN: 0013-936X (2015).

33. Liebezeit, G. & Liebezeit, E. Non-pollen particulates in honey and sugar. eng. **30,** 2136–2140. ISSN: 1944-0049 (2013).

34. Liebezeit, G. & Liebezeit, E. Synthetic particles as contaminants in German beers. eng. **31,** 1574–1578. ISSN: 1944-0049 (2014).

35. Kosuth, M., Mason, S. A. & Wattenberg, E. V. Anthropogenic contamination of tap water, beer, and sea salt. eng. *PloS one* **13,** e0194970. ISSN: 1932-6203 (2018).

36. Mason, S. A., Welch, V. G. & Neratko, J. Synthetic Polymer Contamination in Bottled Water. eng. *Frontiers in chemistry* **6,** 407–407. ISSN: 2296-2646 (2018).

37. Senathirajah, K. *et al.* Estimation of the mass of microplastics ingested – A pivotal first step towards human health risk assessment. *Journal of Hazardous Materials* **404,** 124004. ISSN: 0304-3894. https://www.sciencedirect.com/science/article/pii/S0304389420319944 (2021).

38. Alvarez-Román, R., Naik, A., Kalia, Y., Guy, R. & Fessi, H. Skin penetration and distribution of polymeric nanoparticles. eng. *Journal of controlled release* **99,** 53–62. ISSN: 0168-3659 (2004).

39. Campbell, C. S., Contreras-Rojas, L. R., Delgado-Charro, M. B. & Guy, R. H. Objective assessment of nanoparticle disposition in mammalian skin after topical exposure. eng. *Journal of controlled release* **162,** 201–207. ISSN: 0168-3659 (2012).

40. Lithner, D., Larsson, Å. & Dave, G. Environmental and health hazard ranking and assessment of plastic polymers based on chemical composition. eng. *The Science of the total environment* **409,** 3309–3324. ISSN: 0048-9697 (2011).
41. Ehrlich, S. *et al.* Urinary bisphenol A concentrations and early reproductive health outcomes among women undergoing IVF. eng. *Human reproduction (Oxford)* **27,** 3583–3592. ISSN: 0268-1161 (2012).
42. Miao, M., Yuan, W., Zhu, G., He, X. & Li, D.-K. In utero exposure to bisphenol-A and its effect on birth weight of offspring. eng. **32,** 64–68. ISSN: 0890-6238 (2011).
43. Gregory, M. R. & Ryan, P. G. Pelagic plastics and other seaborne persistent synthetic debris: a review of Southern Hemisphere perspectives. *Marine debris,* 49–66 (1997).
44. *Analysis of nanoplastics and microplastics in food* First edition.. eng. ISBN: 9780429469596 (CRC Press, Boca Raton, FL : 2021).
45. Laist, D. W. in *Marine debris* 99–139 (Springer, 1997).
46. *Plastic Debris in the World's Oceans* https://www.greenpeace.to/greenpeace/wp-content/uploads/2011/05/plastic_ocean_report.pdf (2020).
47. Piccardo, M., Renzi, M. & Terlizzi, A. Nanoplastics in the oceans: Theory, experimental evidence and real world. eng. *Marine pollution bulletin* **157,** 111317–111317. ISSN: 0025-326X (2020).
48. Rossi, G., Barnoud, J. & Monticelli, L. Polystyrene nanoparticles perturb lipid membranes. *The journal of physical chemistry letters* **5,** 241–246 (2014).
49. Forte, M. *et al.* Polystyrene nanoparticles internalization in human gastric adenocarcinoma cells. *Toxicology in Vitro* **31,** 126–136. ISSN: 0887-2333 (2016).
50. Cedervall, T., Hansson, L.-A., Lard, M., Frohm, B. & Linse, S. Food chain transport of nanoparticles affects behaviour and fat metabolism in fish. *PloS one* **7,** e32254 (2012).
51. Pitt, J. A. *et al.* Uptake, tissue distribution, and toxicity of polystyrene nanoparticles in developing zebrafish (Danio rerio). *Aquatic Toxicology* **194,** 185–194. ISSN: 0166-445X (2018).

52. Pitt, J. A. *et al.* Maternal transfer of nanoplastics to offspring in zebrafish (Danio rerio): A case study with nanopolystyrene. *Science of The Total Environment* **643,** 324–334. ISSN: 0048-9697 (2018).

53. van Pomeren, M., Brun, N., Peijnenburg, W. & Vijver, M. Exploring uptake and biodistribution of polystyrene (nano)particles in zebrafish embryos at different developmental stages. *Aquatic Toxicology* **190,** 40–45. ISSN: 0166-445X (2017).

54. Enhanced uptake of BPA in the presence of nanoplastics can lead to neurotoxic effects in adult zebrafish. *Science of The Total Environment* **609,** 1312–1321. ISSN: 0048-9697 (2017).

55. Chen, Q. *et al.* Quantitative investigation of the mechanisms of microplastics and nanoplastics toward zebrafish larvae locomotor activity. *Science of The Total Environment* **584-585,** 1022–1031. ISSN: 0048-9697 (2017).

56. Lee, W. S. *et al.* Bioaccumulation of polystyrene nanoplastics and their effect on the toxicity of Au ions in zebrafish embryos. *Nanoscale* **11,** 3173–3185 (2019).

57. Long-term toxicity of surface-charged polystyrene nanoplastics to marine planktonic species Dunaliella tertiolecta and Artemia franciscana. *Aquatic Toxicology* **189,** 159–169. ISSN: 0166-445X (2017).

58. The toxicity of plastic nanoparticles to green algae as influenced by surface modification, medium hardness and cellular adsorption. *Aquatic Toxicology* **183,** 11–20. ISSN: 0166-445X (2017).

59. González-Fernández, C. *et al.* Do transparent exopolymeric particles (TEP) affect the toxicity of nanoplastics on Chaetoceros neogracile? *Environmental Pollution* **250,** 873–882. ISSN: 0269-7491 (2019).

60. Venâncio, C. *et al.* The effects of nanoplastics on marine plankton: A case study with polymethylmethacrylate. *Ecotoxicology and Environmental Safety* **184,** 109632. ISSN: 0147-6513 (2019).

61. Heinlaan, M. *et al.* Hazard evaluation of polystyrene nanoplastic with nine bioassays did not show particle-specific acute toxicity. *Science of The Total Environment* **707,** 136073. ISSN: 0048-9697 (2020).

62. Baudrimont, M. *et al.* Ecotoxicity of polyethylene nanoplastics from the North Atlantic oceanic gyre on freshwater and marine organisms (microalgae and filter-feeding bivalves). *Environmental Science and Pollution Research* **27,** 3746–3755 (2020).

63. Bhattacharya, P., Lin, S., Turner, J. P. & Ke, P. C. Physical adsorption of charged plastic nanoparticles affects algal photosynthesis. *The Journal of Physical Chemistry C* **114,** 16556–16561 (2010).

64. Teuten, E. L. *et al.* Transport and release of chemicals from plastics to the environment and to wildlife. *Philosophical Transactions of the Royal Society B: Biological Sciences* **364,** 2027–2045 (2009).

65. Bandmann, V., Müller, J. D., Köhler, T. & Homann, U. Uptake of fluorescent nano beads into BY2-cells involves clathrin-dependent and clathrin-independent endocytosis. eng. *FEBS letters* **586,** 3626–3632. ISSN: 0014-5793 (2012).

66. Zhenxia, L., Qingfei, L., Ruijing, L., Junguo, Z. & Wang, G. The distribution and impact of polystyrene nanoplastics on cucumber plants. *Environmental science and pollution research international* **28.** Copyright - © Springer-Verlag GmbH Germany, part of Springer Nature 2020; Last updated - 2021-03-18, 16042–16053 (Apr. 2021).

67. Lian, J. *et al.* Impact of polystyrene nanoplastics (PSNPs) on seed germination and seedling growth of wheat (Triticum aestivum L.) *Journal of Hazardous Materials* **385,** 121620. ISSN: 0304-3894. https://www.sciencedirect.com/science/article/pii/S0304389419315742 (2020).

68. Seinfeld, J. H. *Atmospheric chemistry and physics : from air pollution to climate change* Third edition. eng. ISBN: 9781119221166 (Wiley, Hoboken, New Jersey, 2016).

69. Wlasits, P. J. *On the effect of relative humidity on the activation of aerosol particles in butanol-based condensation particle counters* eng (Wien, 2019).

70. Kulkarni, P., Baron, P. A. & Willeke, K. *Aerosol measurement: principles, techniques, and applications, Third edition* 3rd ed. eng. ISBN: 9781118001660 (John Wiley Sons, Inc, Oxford, 2011).

71. https://moodle.univie.ac.at/pluginfile.php/8900823/mod_resource/content/2/VO2_AerosolBasicRepetition.pdf.

72. Steiner, G. *High resolution mobility spectrometry of molecular ions and their effect on the charging probabilities of airborne particles under bipolar diffusion charging conditions* eng (2011).

73. Knutson, E. & Whitby, K. Aerosol classification by electric mobility: apparatus, theory, and applications. *Journal of Aerosol Science* **6,** 443–451 (1975).

74. Intra, P. & Tippayawong, N. An overview of differential mobility analyzers for size classification of nanometer-sized aerosol particles. *Songklanakarin Journal of Science & Technology* **30** (2008).

75. *GRIMM 5524-X soft X-ray Aerosol Charger* https://www.grimm-aerosol.com/products-en/aerosol-neutralizers/5524-x-soft-x-ray/.

76. *TSI Advanced Aerosol Neutralizer Model 3088 spec sheet* https://tsi.com/getmedia/85d6abad-a56a-4a1f-a61d-1c73983c7e7a/Aerosol%20Neutralizers%203088_A4_5001321_RevE_Web?ext=.pdf.

77. Fuchs, N. On the stationary charge distribution on aerosol particles in a bipolar ionic atmosphere. *Geofisica pura e applicata* **56,** 185–193 (1963).

78. *TSI ULTRAFINE CONDENSATIONPARTICLE COUNTERMODEL 3776 Manual* http://tsi.com/getmedia/e3023b6f-0ba1-4ee2-9986-8d4d86a82f8a/3776_2980346_UCPC-Spec-Sheet-A4?ext=.pdf.

79. *TSI Modell 3776 User Manual by Kenelec* https://www.kenelec.com.au/wp-content/uploads/2016/06/TSI_3776_Ultrafine_Condensation_Particle_Counter_Manual.pdf.

80. *TSI NANO WATER-BASED CONDENSATION PARTICLECOUNTER (N-WCPC)MODEL 3788 Manual* https://tsi.com/getmedia/b3aa9539-222f-4799-a342-ba9ff4510a3b/3788_5001340_Web?ext=.pdf.

81. *TSI Modell 3788 User Manual by Kenelec* https://www.kenelec.com.au/wp-content/uploads/2016/06/TSI_3788_Condensation_Particle_Counter_Manual.pdf.

82. *TSI AEROSOL ELECTROMETERMODEL 3068B user manual* https://tsi.com/getmedia/0273d1d1-1f28-463e-ac6a-cccdaf91d5bc/3068B_Aerosol_Electrometer_A4_5001471_WEB?ext=.pdf.

83. Iida, K., Stolzenburg, M. R. & McMurry, P. H. Effect of Working Fluid on Sub-2 nm Particle Detection with a Laminar Flow Ultrafine Condensation Particle Counter. *Aerosol Science and Technology* **43,** 81–96. eprint: https://doi.org/10.1080/02786820802488194. https://doi.org/10.1080/02786820802488194 (2009).

84. Winkler, P. M. *et al.* Heterogeneous Nucleation Experiments Bridging the Scale from Molecular Ion Clusters to Nanoparticles. *Science* **319,** 1374–1377. ISSN: 0036-8075. eprint: https://science.sciencemag.org/content/319/5868/1374.full.pdf. https://science.sciencemag.org/content/319/5868/1374 (2008).

85. Wlasits, P. J. *et al.* Counting on chemistry: laboratory evaluation of seed-material-dependent detection efficiencies of ultrafine condensation particle counters. *Atmospheric Measurement Techniques* **13,** 3787–3798. https://amt.copernicus.org/articles/13/3787/2020/ (2020).

86. Hanwell, M. D. *et al.* Avogadro: An advanced semantic chemical editor, visualization, and analysis platform. eng. *Journal of cheminformatics* **4,** 17–17. ISSN: 1758-2946. http://avogadro.openmolecules.net. (2012).

87. Atkins, P. W. *Atkins' physical chemistry* Eleventh edition. eng. ISBN: 9780198769866 (Oxford University Press, Oxford, 2018).

88. Reichardt, C. (*Solvents and solvent effects in organic chemistry* 4th ed., updated and enl., [1st repr. (with corr.)]. eng. ISBN: 1-283-30239-X (Wiley-VCH, Weinheim, Germany : 2017).

89. https://www.norrscope.com/wp-content/uploads/2018/12/EHA-EHC-Information.pdf.

90. https://www.sensidyne.com/air-sampling-equipment/calibration-equipment/gilibrator-2/.

91. Wiedensohler, A. An approximation of the bipolar charge distribution for particles in the submicron size range. *Journal of aerosol science* **19,** 387–389 (1988).